PREPARATION AND OPERATIONS OF THE MISSION PERFORMANCE CENTRE (MPC) FOR THE COPERNICUS SENTINEL-3 MISSION

S3-A OLCI Cyclic Performance Report

Cycle No. 026

Start date: 20/12/2017

End date: 16/01/2018

SENTINEL 3

Mission Performance Centre

Ref.: S3MPC.ACR.PR.01-026
Issue: 1.0
Date: 23/01/2018
Contract: 4000111836/14/I-LG

Customer:	ESA	**Document Ref.:**	S3MPC.ACR.PR.01-026
Contract No.:	4000111836/14/I-LG	**Date:**	23/01/2018
		Issue:	1.0

Project:	PREPARATION AND OPERATIONS OF THE MISSION PERFORMANCE CENTRE (MPC) FOR THE COPERNICUS SENTINEL-3 MISSION		
Title:	S3-A OLCI Cyclic Performance Report		
Author(s):	OLCI ESLs		
Approved by:	L. Bourg, OLCI ESL Coordinator	**Authorized by**	Frédéric Rouffi, OPT Technical Performance Manager
Distribution:	ESA, EUMETSAT, S3MPC consortium		
Accepted by ESA	S. Dransfeld, MPC Deputy TO for OPT P. Féménias, MPC TO		
Filename	S3MPC.ACR.PR.01-026 - i1r0 - OLCI Cyclic Report 026.docx		

Disclaimer

The work performed in the frame of this contract is carried out with funding by the European Union. The views expressed herein can in no way be taken to reflect the official opinion of either the European Union or the European Space Agency.

Changes Log

Version	Date	Changes
1.0	23/01/2018	First Version

List of Changes

Version	Section	Answers to RID	Changes

Table of content

TABLE OF CONTENT IV

LIST OF FIGURES V

1 PROCESSING BASELINE VERSION 1

2 INSTRUMENT MONITORING 2

2.1 CCD TEMPERATURES 2
2.2 RADIOMETRIC CALIBRATION 3
2.2.1 Dark Offsets [OLCI-L1B-CV-230] 5
2.2.2 Instrument response and degradation modelling [OLCI-L1B-CV-250] 11
2.2.3 Ageing of nominal diffuser [OLCI-L1B-CV-240] 19
2.2.4 Updating of calibration ADF [OLCI-L1B-CV-260] 19
2.2.5 Radiometric Calibrations for sun azimuth angle dependency and Yaw Manoeuvres for Solar Diffuser on-orbit re-characterization [OLCI-L1B-CV-270 and OLCI-L1B-CV-280] 19
2.3 SPECTRAL CALIBRATION [OLCI-L1B-CV-400] 19
2.4 SIGNAL TO NOISE ASSESSMENT [OLCI-L1B-CV-620] 19
2.4.1 SNR from Radiometric calibration data 19
2.4.2 SNR from EO data 22
2.5 GEOMETRIC CALIBRATION/VALIDATION 22

3 OLCI LEVEL 1 PRODUCT VALIDATION 27

3.1 [OLCI-L1B-CV-300], [OLCI-L1B-CV-310] – RADIOMETRIC VALIDATION 27
3.1.1 S3ETRAC Service 27
3.1.2 Radiometric validation with DIMITRI 28
3.1.3 Radiometric validation with OSCAR 36
3.2 [OLCI-L1B-CV-320] – RADIOMETRIC VALIDATION WITH LEVEL 3 PRODUCTS 36

4 LEVEL 2 LAND PRODUCTS VALIDATION 37

4.1 [OLCI-L2LRF-CV-300] 37
4.2 [OLCI-L2LRF-CV-410 & OLCI-L2LRF-CV-420] – CLOUD MASKING & SURFACE CLASSIFICATION FOR LAND PRODUCTS 37

5 LEVEL 2 WATER PRODUCTS VALIDATION 38

5.1 [OLCI-L2-CV-210, OLCI-L2-CV-220] – VICARIOUS CALIBRATION OF THE NIR AND VIS BANDS 38
5.2 [OLCI-L2WLR-CV-300, OLCI-L2WLR-CV-310, OLCI-L2WLR-CV-32, OLCI-L2WLR-CV-330, OLCI-L2WLR-CV-340, OLCI-L2WLR-CV-350, OLCI-L2WLR-CV-360 AND OLCI-L2WLR-CV-370] – LEVEL 2 WATER-LEAVING REFLECTANCE PRODUCT VALIDATION 38
5.3 [OLCI-L2WLR-CV-510 & 520] – CLOUD MASKING & SURFACE CLASSIFICATION FOR WATER PRODUCTS 51
5.4 [OLCI-L2WLR-CV530] VALIDATION OF AEROSOL PRODUCT 51
5.5 [OLCI-L2WLR-CV-380] DEVELOPMENT OF CALIBRATION, PRODUCT AND SCIENCE ALGORITHMS 51

6 VALIDATION OF INTEGRATED WATER VAPOUR OVER LAND & WATER 52

7 LEVEL 2 SYN PRODUCTS VALIDATION 53

7.1 [SYN-L2-CV-100] 53

8 EVENTS 54

9 APPENDIX A 55

List of Figures

Figure 1: long term monitoring of CCD temperatures using minimum value (top), time averaged values (middle), and maximum value (bottom) provided in the annotations of the Radiometric Calibration Level 1 products, for the Shutter frames, all radiometric calibrations so far. ---------- 2

Figure 2: Same as Figure 1 for diffuser frames. ---------- 3

Figure 3: Sun azimuth angles during acquired Radiometric Calibrations (diffuser frame) on top of nominal yearly cycle (black curve). Diffuser 1 with diamonds, diffuser 2 with crosses, 2016 acquisitions in blue, 2017 in green, 2018 in red. ---------- 4

Figure 4: Sun geometry during radiometric Calibrations on top of characterization ones (diffuser frame) 4

Figure 5: Dark Offset table for band Oa06 with (red) and without (black) HEP filtering (Radiometric Calibration of 22 July 2017). The strong HEP event near pixel 400 has been detected and removed by the HEP filtering. ---------- 5

Figure 6: Dark Offset for band Oa1 (top) and Oa21 (bottom), all radiometric calibrations so far except the first one (orbit 183) for which the instrument was not thermally stable yet. ---------- 6

Figure 7: map of periodic noise for the 5 cameras, for band Oa21. X-axis is detector number (East part, from 540 to 740, where the periodic noise occurs), Y-axis is the orbit number. The counts have been corrected from the west detectors mean value (not affected by periodic noise) in order to remove mean level gaps and consequently to have a better visualisation of the long term evolution of the periodic noise structure. Periodic noise amplitude is high in camera 2, 3 and 4. It is lower in camera 4 and small in camera 1. ---------- 7

Figure 8: same as Figure 7 for smear band. ---------- 7

Figure 9: Dark levels for smear band camera 5, for (left plot) first 30 WEST detectors including virtual and blind pixels, (right plot) last 30 EAST detectors including blind pixels. The colour of the curves is linked to the orbit number, from the beginning of the mission in black, to the last CALs in red. We see on the right plot that the shape of the PN for the CALs at orbit ≥ 9664 has been modified by the reset of the OLCI instrument of orbit 9572 (Cycle #25). ---------- 8

Figure 10: Dark levels for smear band camera 4, for (upper plot) all detectors, (lower left plot) first 30 WEST detectors including virtual and blind pixels, (lower right plot) last 30 EAST detectors including blind pixels. The colour of the curves is linked to the orbit number, from the beginning of the mission in black, to the last CALs in red. We see that a hot pixel appeared in the last 2 CALs (cycle 26) in “blind pixel East” region which induced, for this camera and band, an offset of the “mean dark level” of about 0.5 counts.9

Figure 11: Dark Current for band Oa1 (top) and Oa21 (bottom), all radiometric calibrations so far except the first one (orbit 183) for which the instrument was not thermally stable yet. ----------10

Figure 12: left column: ACT mean on 400 first detectors of Dark Current coefficients for spectral band Oa01 (top) and Oa21 (bottom). Right column: same as left column but for Standard deviation instead of mean. We see an increase of the DC level as a function of time especially for band Oa21. A possible

explanation could be the increase of the number of hot pixels which is more important in Oa21 because this band is made of more CCD lines than band Oa01 and thus receives more cosmic rays impacts. It is known that cosmic rays degrade the structure of the CCD, generating more and more hot pixels at long term scales. ----------10

Figure 13: Gain Coefficients for band Oa1 (top) and Oa21 (bottom), all diffuser 1 radiometric calibrations so far except the first one (orbit 183) for which the instrument was not thermally stable yet. ----------11

Figure 14: camera averaged gain relative evolution with respect to “best geometry” calibration (22/11/2016), as a function of elapsed time since launch; one curve for each band (see colour code on plots), one plot for each module. The star tracker anomaly fix (6/04/16) is represented by a vertical red dashed line. ----------12

Figure 15: RMS performance of the Gain Model of current Processing Baseline as a function of orbit.---13

Figure 16: RMS performance of the Gain Model of previous Processing Baseline as a function of orbit. -13

Figure 17: Camera-averaged instrument evolution since channel programming change (25/04/2016) and up to most recent calibration (10/01/2018) versus wavelength. ----------14

Figure 18: For the 5 cameras: Evolution model performance, as camera-average and standard deviation of ratio of Model over Data vs. wavelength, for each orbit of the test dataset, including 9 calibrations in extrapolation, with a colour code for each calibration from blue (oldest) to red (most recent).----------15

Figure 19: Evolution model performance, as ratio of Model over Data vs. pixels, all cameras side by side, over the whole current calibration dataset (since instrument programing update), including 9 calibrations in extrapolation, channels Oa1 to Oa6. ----------16

Figure 20: same as Figure 14 for channels Oa7 to Oa14. ----------17

Figure 21: same as Figure 19 for channels Oa15 to Oa21.----------18

Figure 22: Signal to Noise ratio as a function of the spectral band for the 5 cameras. These results have been computed from radiometric calibration data. All calibrations except first one (orbit 183) are presents with the colours corresponding to the orbit number (see legend). The SNR is very stable with time: the curves for all orbits are almost superimposed. The dashed curve is the ESA requirement. -----20

Figure 23: long-term stability of the SNR estimates from Calibration data, example of channel Oa1. -----21

Figure 24: histograms of geolocation errors for the along-track (left) and across-track (right) directions, examples of 22/12/2017 (top) and 15/01/2018 (bottom). ----------23

Figure 25: georeferencing error in along-track (left) and across-track (right) directions for all the GCPs, examples of 22/12/2017 (top) and 15/01/2018 (bottom). ----------24

Figure 26: time series of geolocation errors for the along-track (blue) and across-track (red) directions over 18.7 months. ----------24

Figure 27: validation of the updated Geometric Calibration Models: residual geolocation error using new models (left) compared to those using current baseline on same data set. The validation data set extends from 15/10 to 29/11/2017, i.e. outside the ESTEC training set. ----------25

Figure 28: time series f along-track (left) and across-track (right) geolocation performance on the reprocessed data set. Central curves are the RMS performance while upper and lower ones are RMS ±1 standard deviation.----------26

Figure 29: summary of S3ETRAC products generation for OLCI (number of OLCI L1 products Ingested, yellow – number of S3ETRAC extracted products generated, blue – number of S3ETRAC runs without generation of output product (data not meeting selection requirements), green – number of runs ending in error, red, one plot per site type). ----------28

Figure 30: Time-series of the elementary ratios (observed/simulated) signal from S3A/OLCI for (top to bottom) bands Oa03, Oa8 and Oa17 respectively over Six PICS Cal/Val sites. Dashed-green and orange lines indicate the 2% and 5% respectively. Error bars indicate the desert methodology uncertainty.-----30

Figure 31: The estimated gain values for S3A/OLCI over the 6 PICS sites identified by CEOS over the period April 2016 – October 2017 as a function of wavelength. Dashed-green and orange lines indicate the 2% and 5% respectively. Error bars indicate the desert methodology uncertainty. ----------31

Figure 32: Time-series of the elementary ratios (observed/simulated) signal from (black) S2A/MSI, (blue) S3A/OLCI, and (Cyan) MODIS-A for band Oa17 (865nm) over the LIBYA4 site. Dashed-green and orange lines indicate the 2% and 5% respectively. Error bars indicate the desert methodology uncertainty.-----32

Figure 33: The estimated gain values (observed-signal /simulated-signal) averaged over different period (OLCI: 20160331-20180105; MSI-A: 20150701-20180105; MODIS-A: 20150101-20180101 and OLI: 20150701-20170330) over PICS as function of wavelength. The number of used-acquisitions from each sensor over the averaging period is indicated in the plot-legend.----------33

Figure 34: The estimated gain values for S3A/OLCI over the 6 Ocean CalVal sites (Atl-NW_Optimum, Atl-SW_Optimum, Pac-NE_Optimum, Pac-NW_Optimum, SPG_Optimum and SIO_Optimum) over the period December 2016 – December 2017 as a function of wavelength. Dashed-green, and orange lines indicate the 2%, 5% respectively. Error bars indicate the methodology uncertainty. ----------33

Figure 35: The estimated gain values for S3A/OLCI from Glint, Rayleigh and PICS over the period April 2016 – November 2017 for PICS and December 2016- December 2017 for Glint and December 2016-November 2017 for Rayleigh methods as a function of wavelength. We use the gain value of Oa8 from PICS method as reference gain for Glint. Dashed-green and orange lines indicate the 2% and 5% respectively. Error bars indicate the methods uncertainties.----------34

Figure 36: Time-series of the elementary ratios (observed/simulated) signal from S3A/OLCI products (REP006: July 2016 – December 2017) for (top to bottom) bands Oa08 and Oa17 respectively over Six PICS Cal/Val sites. Dashed-green and orange lines indicate the 2% and 5% respectively. Error bars indicate the desert methodology uncertainty. ----------35

Figure 37: The estimated gain values for S3A/OLCI from PICS, Glint and Rayleigh methods over the reprocessed products (REP006: July 2016 – July 2017; Dec 2017 for PICS) as a function of wavelength. We use the gain value of Oa8 from Rayleigh method as reference gain for Glint. Dashed-green and orange lines indicate the 2% and 5% respectively. Error bars indicate the methods uncertainties. --------36

Figure 38: MOBY time series over current report period ----------40

Figure 39: Location of the sites around the HLT (top left), the GDLT (top right) and the LISCO platform (bottom).----------42

Figure 40: Normalized water leaving-reflectance (ρ_{WN}) averaged over 3 and 5 days from (green) OLCI and (red) the in-situ measurements from GDLT on the 13 & 31/07, 24/08 in 2017 (left) and HLT on the 7, 14 & 27/07, 14/08, 23/09 in 2017 (right). Applied OLCI flags (top) RHWNEG_b and (bottom) RHWNEG_b and WQSF_lsb_HIGHRW are raised----------43

Figure 41: Regression plots of ρ_{WN} (OLCI/InSitu) over the 9*9 pixels matchups for GDLT on the 13 & 31/07, 24/08 of 2017 (left) and HLT on the 7, 14 & 27/07, 14/08, 23/09 of 2017 (right). Applied OLCI flags (top) RHWNEG_b and (bottom) RHWNEG_b and WQSF_lsb_HIGHRW are raised. ----------45

Figure 42: Absolute relative percent difference of OLCI L2 ρ_{WN} estimations with in-situ measurements from GDLT on the 13 & 31/07, 24/08 of 2017 (left) and HLT on the 7, 14 & 27/07, 14/08 and 23/09 of 2017 (right). Applied OLCI flags (top) RHWNEG_b and (bottom) RHWNEG_b and WQSF_lsb_HIGHRW are raised. ----------45

Figure 43: Total suspended matter concentration, estimated from OLCI L2 around GDLT on the 31/07/2017 (top) and HLT on the 14/08/2017 (bottom). ----------47

Figure 44: Normalized water leaving-reflectance (ρWN) averaged over OLCI and the in-situ measurements from LISCO on the 09/07, 01 & 31/08, 04 & 08/09, 21 & 28/11 of 2017. Applied OLCI flags (left) RHWNEG_b and (right) RHWNEG_b and WQSF_lsb_HIGHRW are raised----------48

Figure 45: Regression plots over the 5x5 matchups for OLCI L2 and the in-situ measurements of ρWN at LISCO on the 09/07, 01 & 31/08, 04 & 08/09, 21 & 28/11 of 2017. Applied OLCI flags (left) RHWNEG_b and (right) RHWNEG_b and WQSF_lsb_HIGHRW are raised.----------49

Figure 46: Absolute relative percent difference of OLCI L2 ρWN estimations with in-situ measurements from LISCO on the 09/07, 01 & 31/08, 04 & 08/09, 21 & 28/11 of 2017. Applied OLCI flags (left) RHWNEG_b and (right) RHWNEG_b and WQSF_lsb_HIGHRW are raised----------49

Figure 47: Total suspended matter concentration, estimated from OLCI L2 around LISCO on the 21/11/2017----------50

1 Processing Baseline Version

IPF	IPF / Processing Baseline version	Date of deployment
OL1	06.07 / 2.23	CGS: 05/07/2017 13:00 UTC (NRT) PAC: 05/07/2017 12:50 UTC (NTC)
OL2	06.11 / 2.23	CGS: 11/10/2017 08:53 UTC (NRT) PAC: 11/10/2017 08:15 UTC (NTC)
SY2	06.12 / 2.26	PAC: 11/01/2018 10:52 UTC
SY2_VGS	06.12 / 2.26	PAC: 11/01/2018 10:52 UTC

2 Instrument monitoring

2.1 CCD temperatures

The monitoring of the CCD temperatures is based on MPMF data extractions not yet operational. In the meantime, we monitor the CCD temperatures on the long-term using Radiometric Calibration Annotations (see Figure 1). Variations are very small (0.09 C peak-to-peak) and no trend can be identified. Data from current cycle (rightmost data points) do not show any specificity.

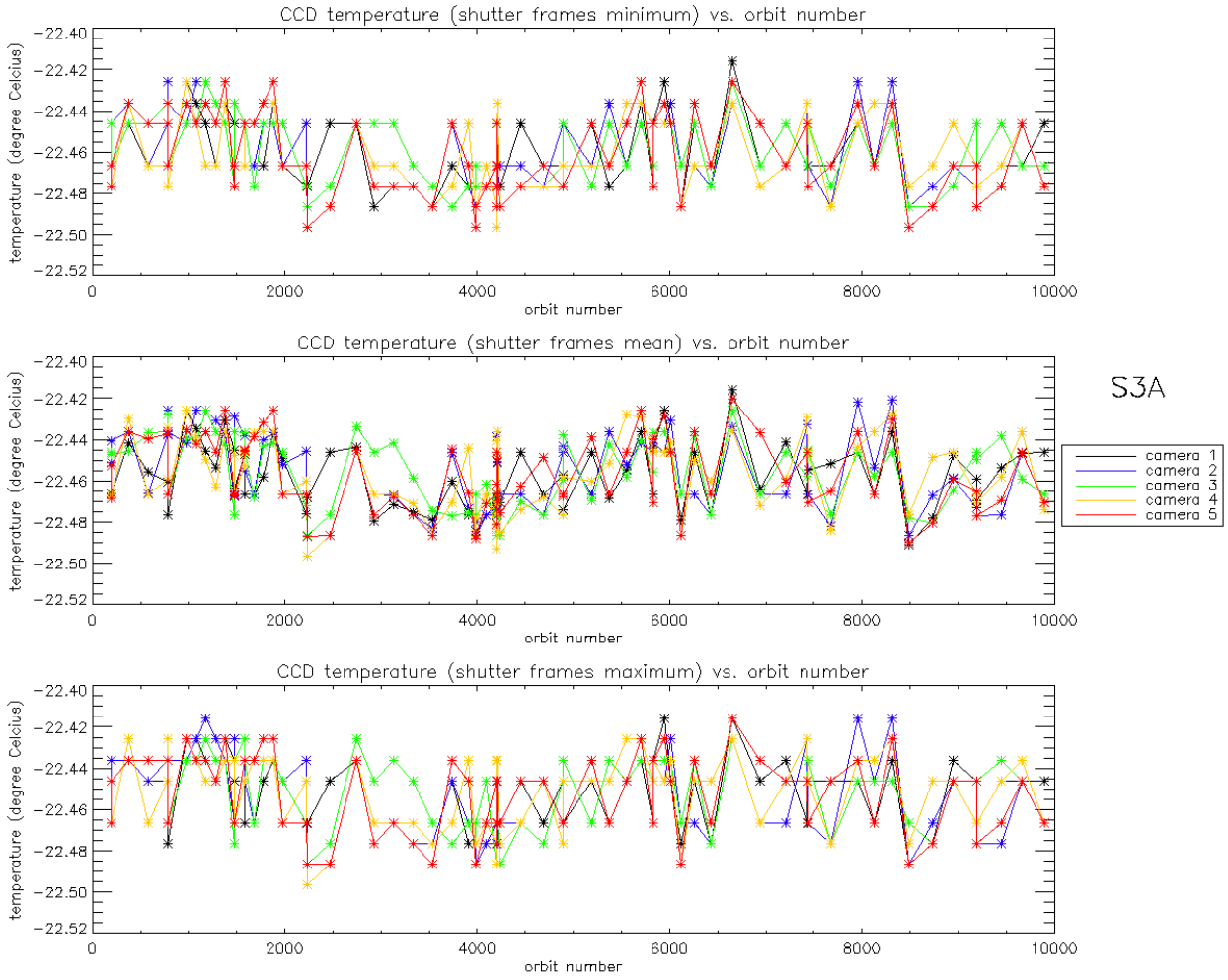

Figure 1: long term monitoring of CCD temperatures using minimum value (top), time averaged values (middle), and maximum value (bottom) provided in the annotations of the Radiometric Calibration Level 1 products, for the Shutter frames, all radiometric calibrations so far.

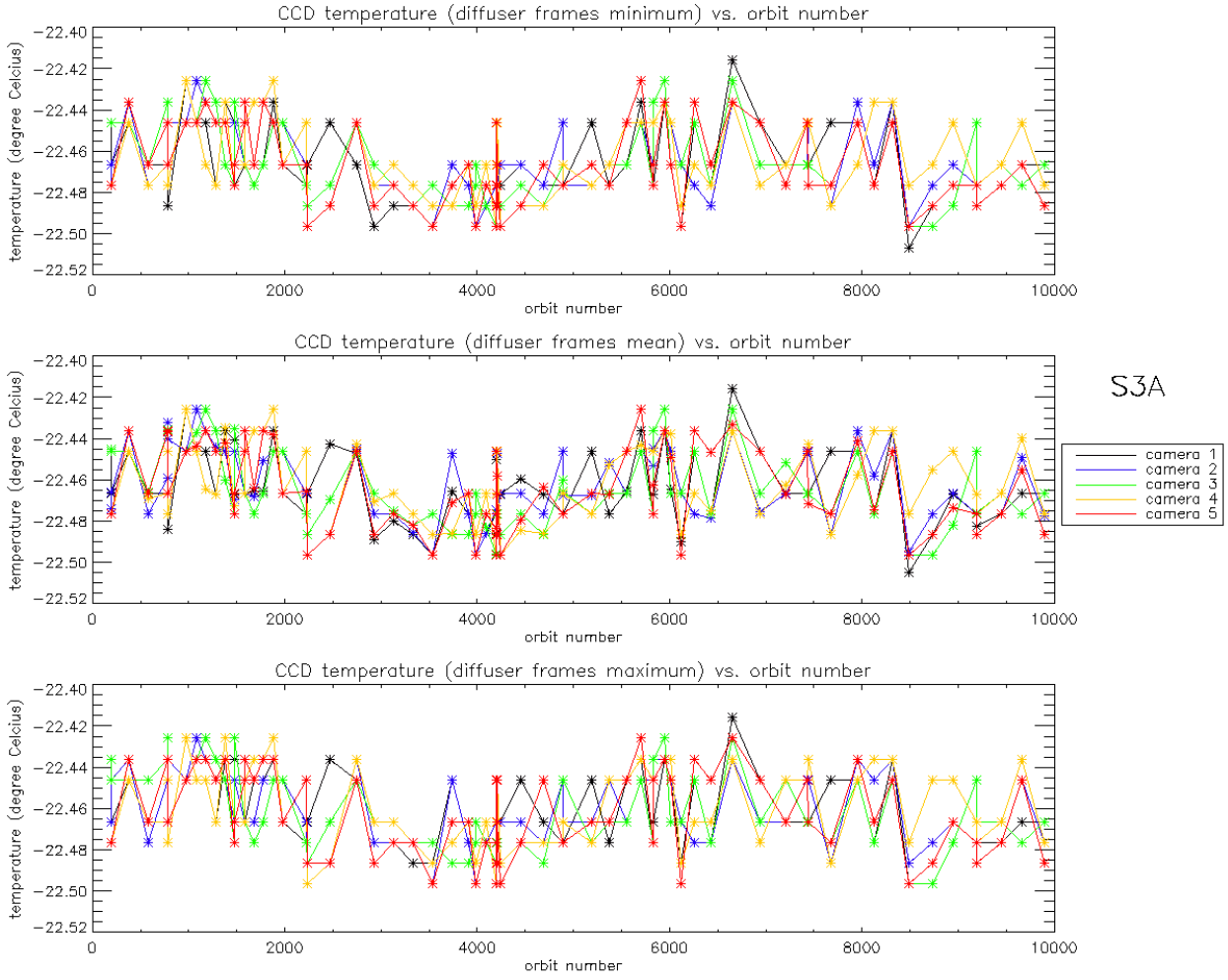

Figure 2: Same as Figure 1 for diffuser frames.

2.2 Radiometric Calibration

Two OLCI Radiometric Calibration Sequences have been acquired during Cycle 026:

- S01 sequence (diffuser 1) on 25/12/2017 12:41 to 12:43 (absolute orbit 9664)
- S01 sequence (diffuser 1) on 10/01/2018 19:09 to 19:11 (absolute orbit 9896)

The acquired Sun azimuth angles are presented on below, on top of the nominal values without Yaw Manoeuvre (i.e. with nominal Yaw Steering control of the satellite).

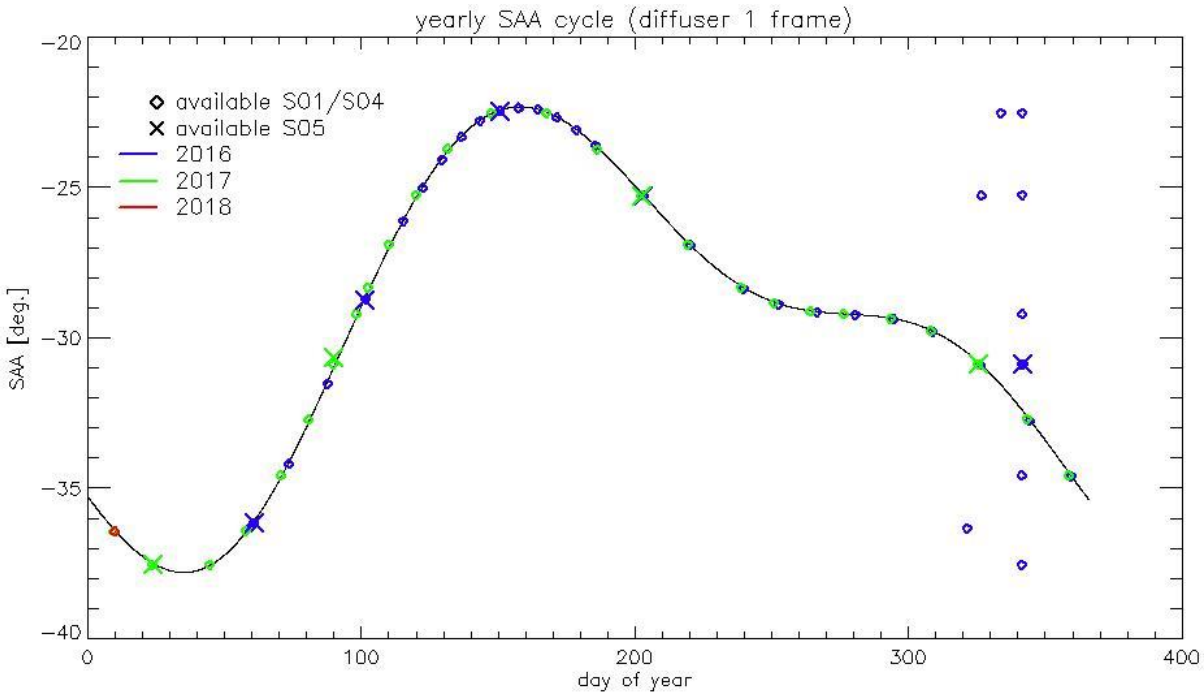

Figure 3: Sun azimuth angles during acquired Radiometric Calibrations (diffuser frame) on top of nominal yearly cycle (black curve). Diffuser 1 with diamonds, diffuser 2 with crosses, 2016 acquisitions in blue, 2017 in green, 2018 in red.

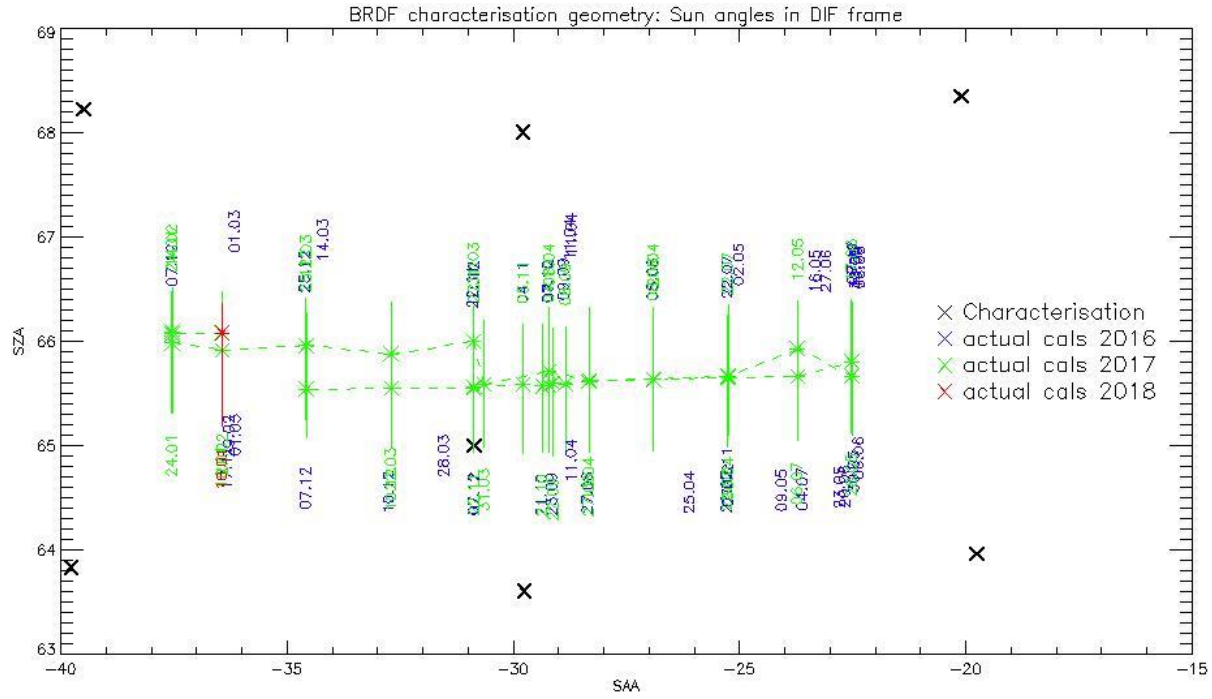

Figure 4: Sun geometry during radiometric Calibrations on top of characterization ones (diffuser frame)

This section presents the overall monitoring of the parameters derived from radiometric calibration data and highlights, if present, specificity of current cycle data.

2.2.1 Dark Offsets [OLCI-L1B-CV-230]

Note about the High Energy Particles:

The filtering of High Energy Particle (HEP) events from radiometric calibration data has been implemented (for shutter frames only) in a post processor, allowing generating Dark Offset and Dark Current tables computed on filtered data. The post-processor starts from IPF intermediate data (corrected counts), applies the HEP detection and filtering and finally computes the Dark Offset and Dark Current tables the same way as IPF. An example of the impact of HEP filtering is given in Figure 5.

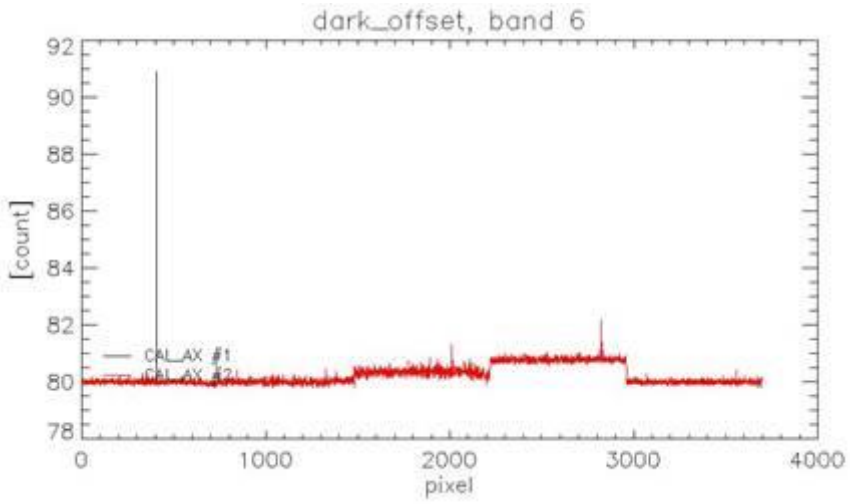

Figure 5: Dark Offset table for band Oa06 with (red) and without (black) HEP filtering (Radiometric Calibration of 22 July 2017). The strong HEP event near pixel 400 has been detected and removed by the HEP filtering.

All results presented below in this section have been obtained using the HEP filtered Dark Offset and Dark Current tables.

Dark offsets

Dark offsets are continuously affected by the global offset induced by the Periodic Noise on the OCL convergence. Current Cycle calibrations are affected the same way as others. The amplitude of the shift varies with band and camera from virtually nothing (e.g. camera 2, band 0a1) to up to 5 counts (Oa21, camera 3). The Periodic Noise itself comes on top of the global shift with its known signature: high frequency oscillations with a rapid damp. This effect remains more or less stable with time in terms of amplitude, frequency and decay length, but its phase varies with time, introducing the global offset mentioned above.

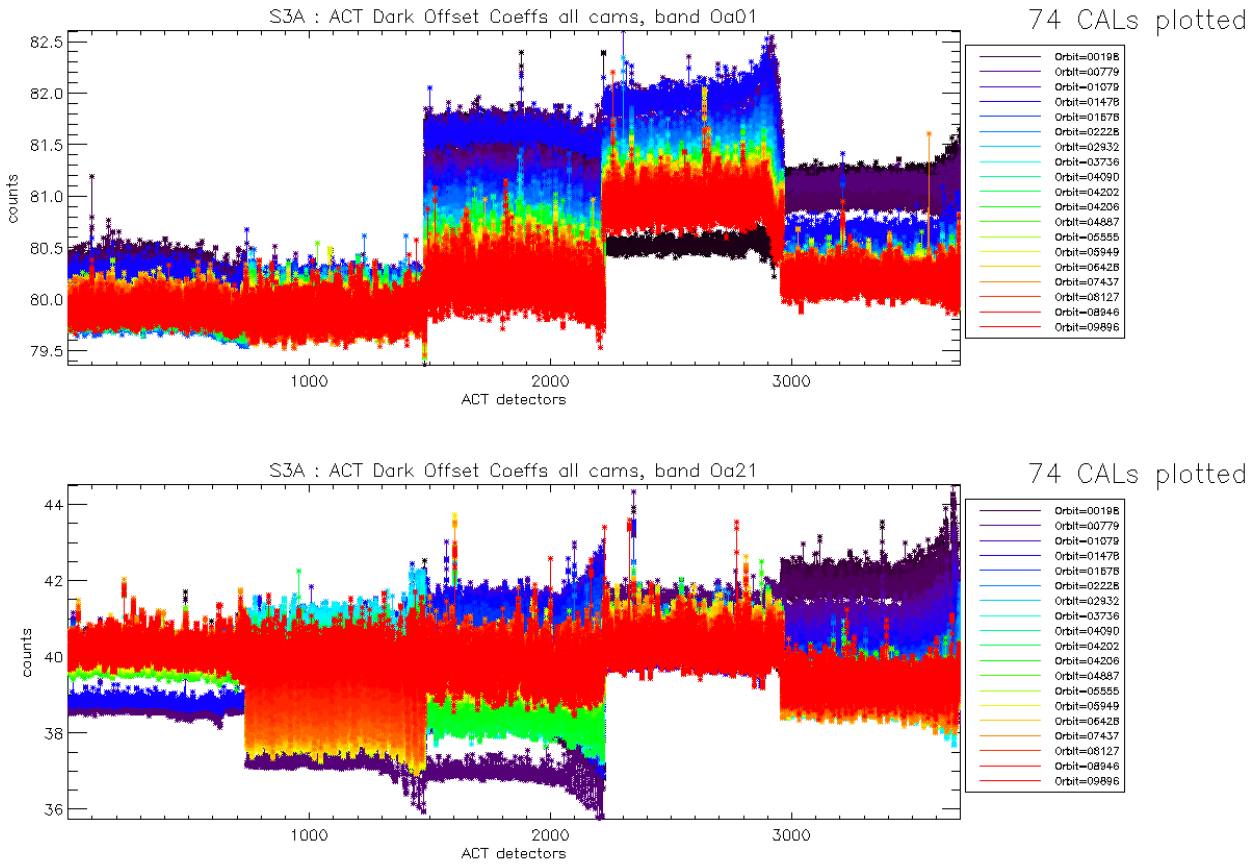

Figure 6: Dark Offset for band Oa1 (top) and Oa21 (bottom), all radiometric calibrations so far except the first one (orbit 183) for which the instrument was not thermally stable yet.

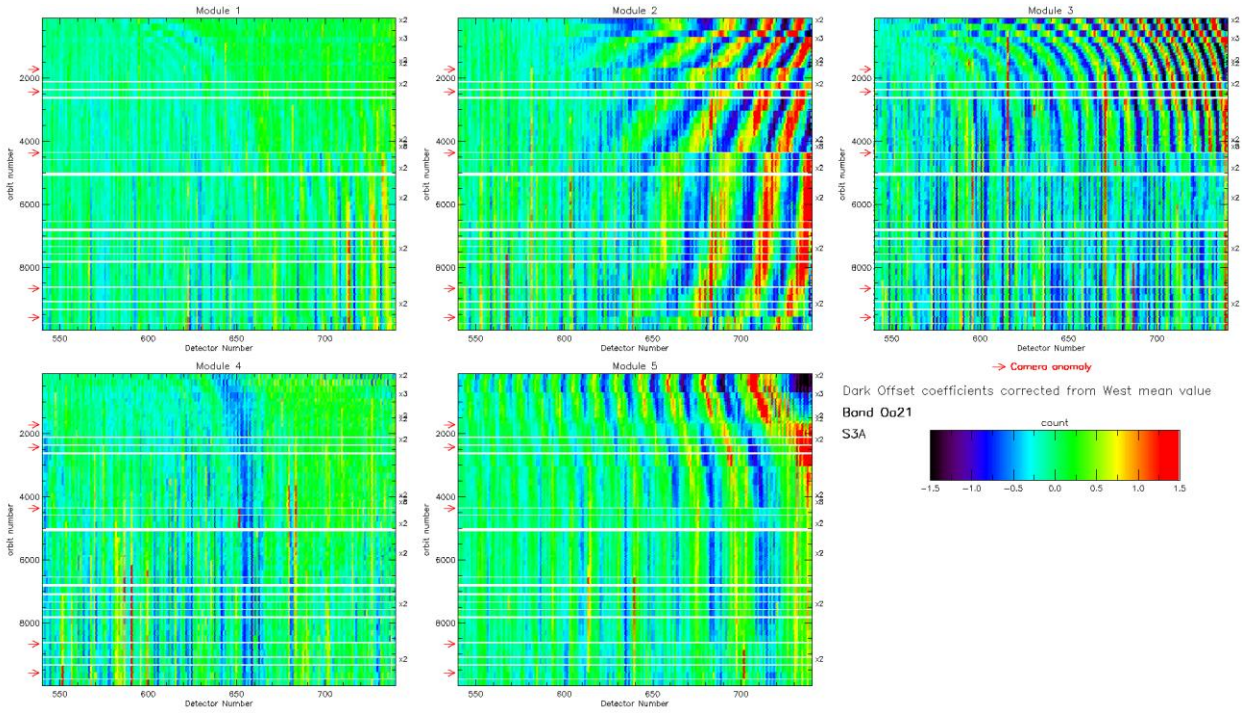

Figure 7: map of periodic noise for the 5 cameras, for band Oa21. X-axis is detector number (East part, from 540 to 740, where the periodic noise occurs), Y-axis is the orbit number. The counts have been corrected from the west detectors mean value (not affected by periodic noise) in order to remove mean level gaps and consequently to have a better visualisation of the long term evolution of the periodic noise structure. Periodic noise amplitude is high in camera 2, 3 and 4. It is lower in camera 4 and small in camera 1.

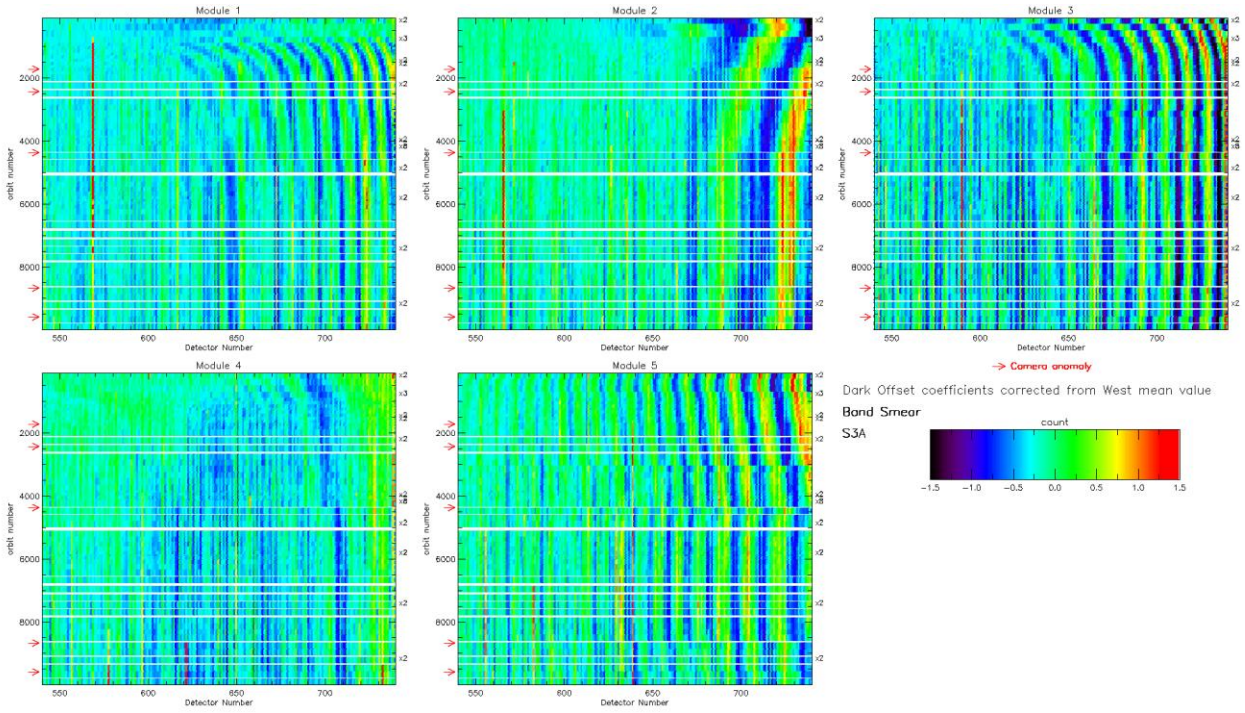

Figure 8: same as Figure 7 for smear band.

Figure 7 and Figure 8 show the so-called 'map of periodic noise' in the 5 cameras, for respectively band 21 and smear band. These maps have been computed from the dark offsets after removal of the mean level of the WEST detectors (not impacted by PN) in order to remove mean level gaps and consequently to highlight the shape of the PN. Maps are focused on the last 200 EAST detectors where PN occurs. We see that the reset of the OLCI instrument performed on 19 DEC 2017,, orbit 9572 (cycle #25) ,following a camera anomaly, had a significant impact on the shape of the PN. The most impacted band is Oa21 in camera 2, as well as, to a lesser extent smear band , camera 5 (see Figure 9).

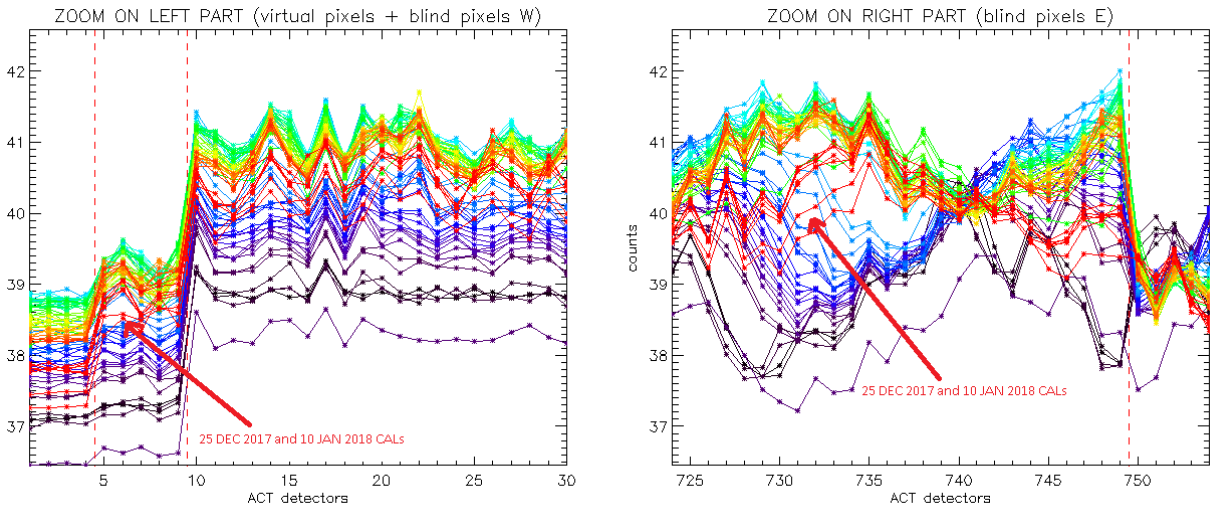

Figure 9: Dark levels for smear band camera 5, for (left plot) first 30 WEST detectors including virtual and blind pixels, (right plot) last 30 EAST detectors including blind pixels. The colour of the curves is linked to the orbit number, from the beginning of the mission in black, to the last CALs in red. We see on the right plot that the shape of the PN for the CALs at orbit ≥ 9664 has been modified by the reset of the OLCI instrument of orbit 9572 (Cycle #25).

Finally we noticed the appearance of a "hot pixel" in the "blind pixel EAST" region for smear band camera 4 in the last 2 CALs. As the OCL convergence is based on this group of blind pixels, this hot pixel induced an offset of about -0.5 counts in the dark mean level. This is illustrated in Figure 10. It is possible that this new hot pixel is not related with the instrument anomaly/reset of 19 DEC 2017.

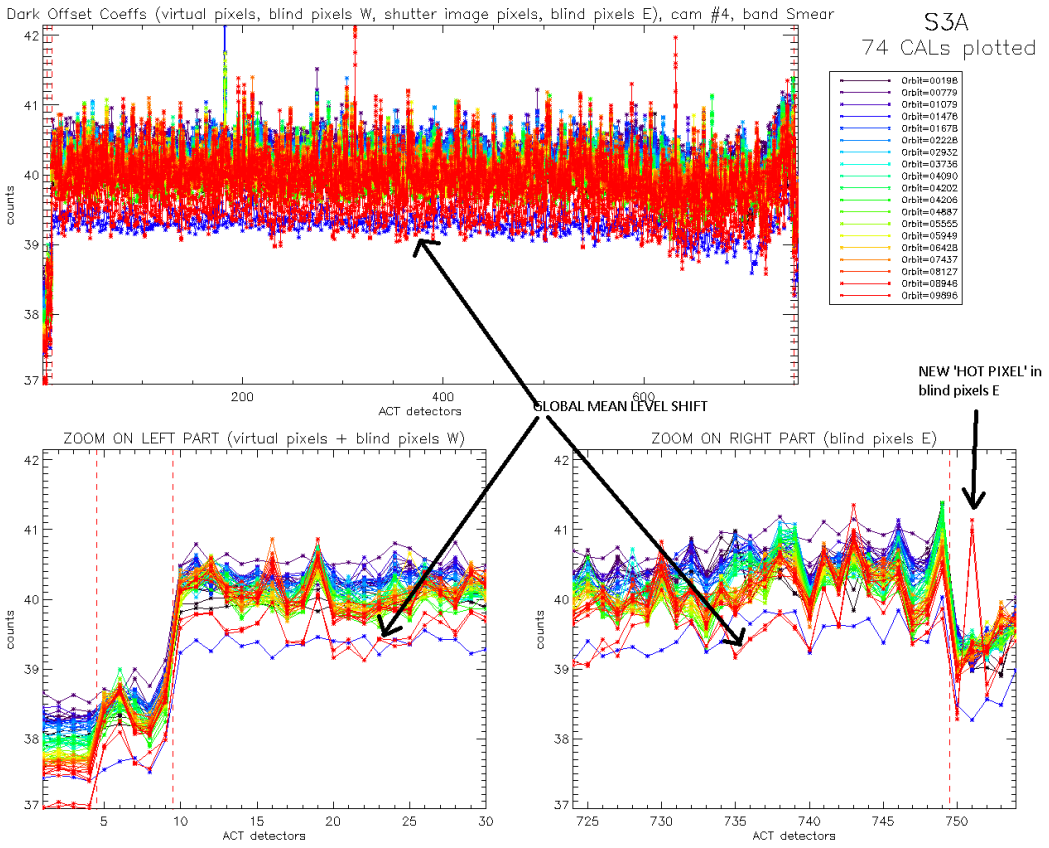

Figure 10: Dark levels for smear band camera 4, for (upper plot) all detectors, (lower left plot) first 30 WEST detectors including virtual and blind pixels, (lower right plot) last 30 EAST detectors including blind pixels. The colour of the curves is linked to the orbit number, from the beginning of the mission in black, to the last CALs in red. We see that a hot pixel appeared in the last 2 CALs (cycle 26) in "blind pixel East" region which induced, for this camera and band, an offset of the "mean dark level" of about 0.5 counts.

Based on the results presented in Figure 8, Figure 9 and Figure 10, we recommend that the CAL_AX used in PDGS is updated, as soon as possible, with a dark offset table and a dark current table computed from a Calibration sequence posterior to the December 2017-anomaly. This will be implemented at the next PB update (foreseen in end of January or early February).

Dark Currents

Dark Currents are not affected by the global offset of the Dark Offsets, thanks to the clamping to the average blind pixels value. However, the oscillations of Periodic Noise remain visible. There is no significant evolution of this parameter during the current cycle.

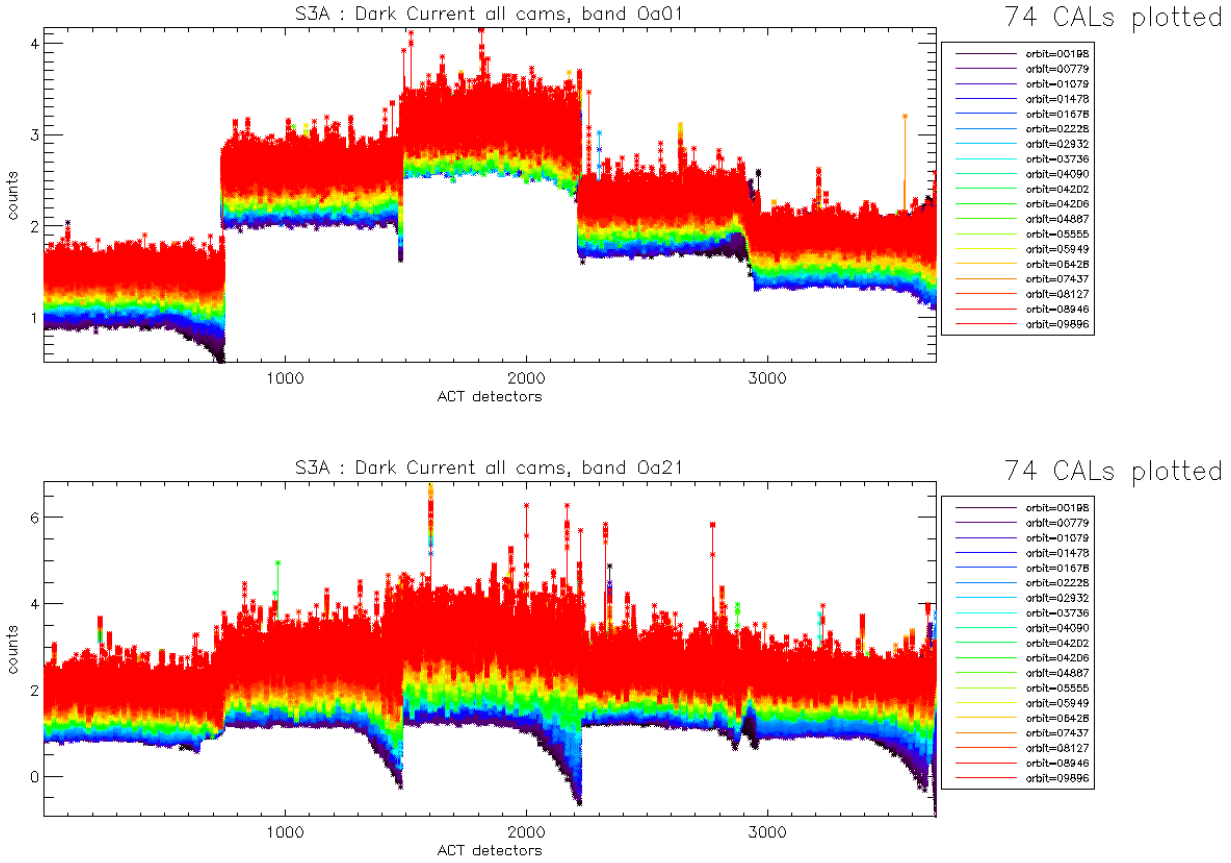

Figure 11: Dark Current for band Oa1 (top) and Oa21 (bottom), all radiometric calibrations so far except the first one (orbit 183) for which the instrument was not thermally stable yet.

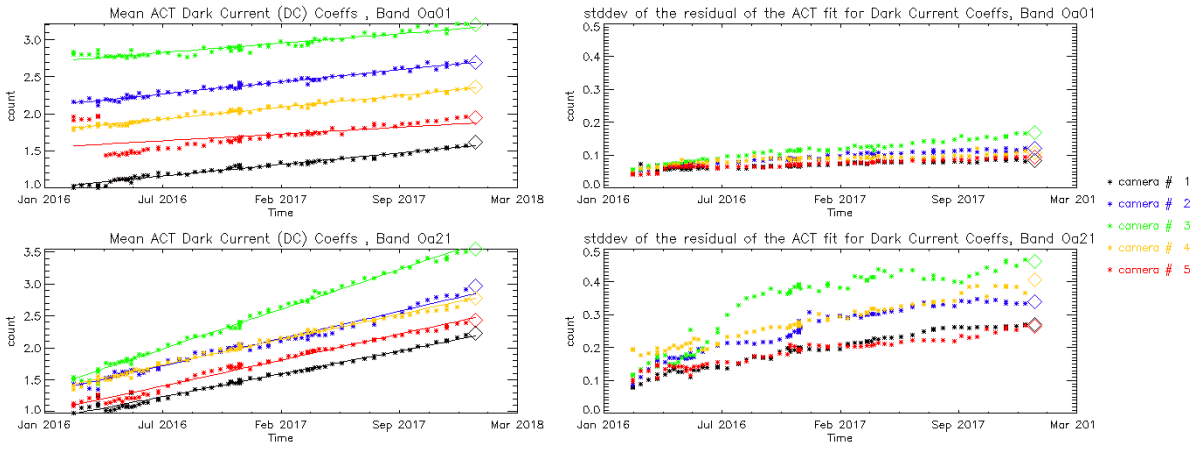

Figure 12: left column: ACT mean on 400 first detectors of Dark Current coefficients for spectral band Oa01 (top) and Oa21 (bottom). Right column: same as left column but for Standard deviation instead of mean. We see an increase of the DC level as a function of time especially for band Oa21. A possible explanation could be the increase of the number of hot pixels which is more important in Oa21 because this band is made of more CCD lines than band Oa01 and thus receives more cosmic rays impacts. It is known that cosmic rays degrade the structure of the CCD, generating more and more hot pixels at long term scales.

2.2.2 Instrument response and degradation modelling [OLCI-L1B-CV-250]

2.2.2.1 Instrument response monitoring

Figure 13 below shows the gain coefficients of every pixel for two OLCI channels, Oa1 (400 nm) and Oa21 (1020 nm), highlighting the significant evolution of the instrument response since early mission.

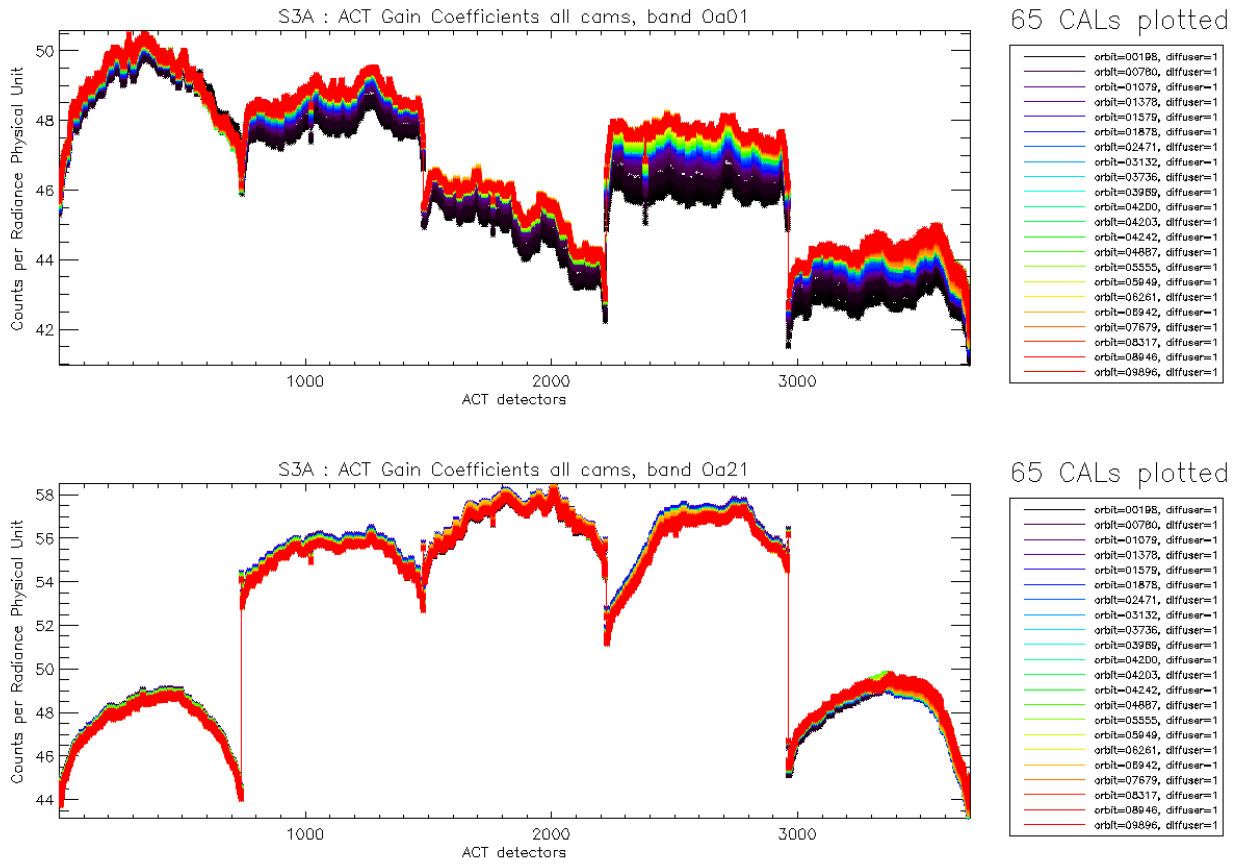

Figure 13: Gain Coefficients for band Oa1 (top) and Oa21 (bottom), all diffuser 1 radiometric calibrations so far except the first one (orbit 183) for which the instrument was not thermally stable yet.

The gains plotted in Figure 13, however are derived using the ground BRDF model – as the only one available in the operational processing software so far – which is known to suffer from illumination geometry dependent residual errors (see previous Cyclic Reports for more details). Consequently they are post-processed to replace the ground BRDF model by the in-flight version, based on Yaw Manoeuvres data, prior to determine the radiometric evolution.

Figure 14 displays a summary of the time evolution derived from post-processed gains: the cross-track average of the BRDF corrected gains is plotted as a function of time, for each module, relative to a given reference calibration (the 12/12/2016). It shows that, if a significant evolution occurred during the early mission, the trends tend to stabilize, with the exception of band 1 of camera 1 and 4.

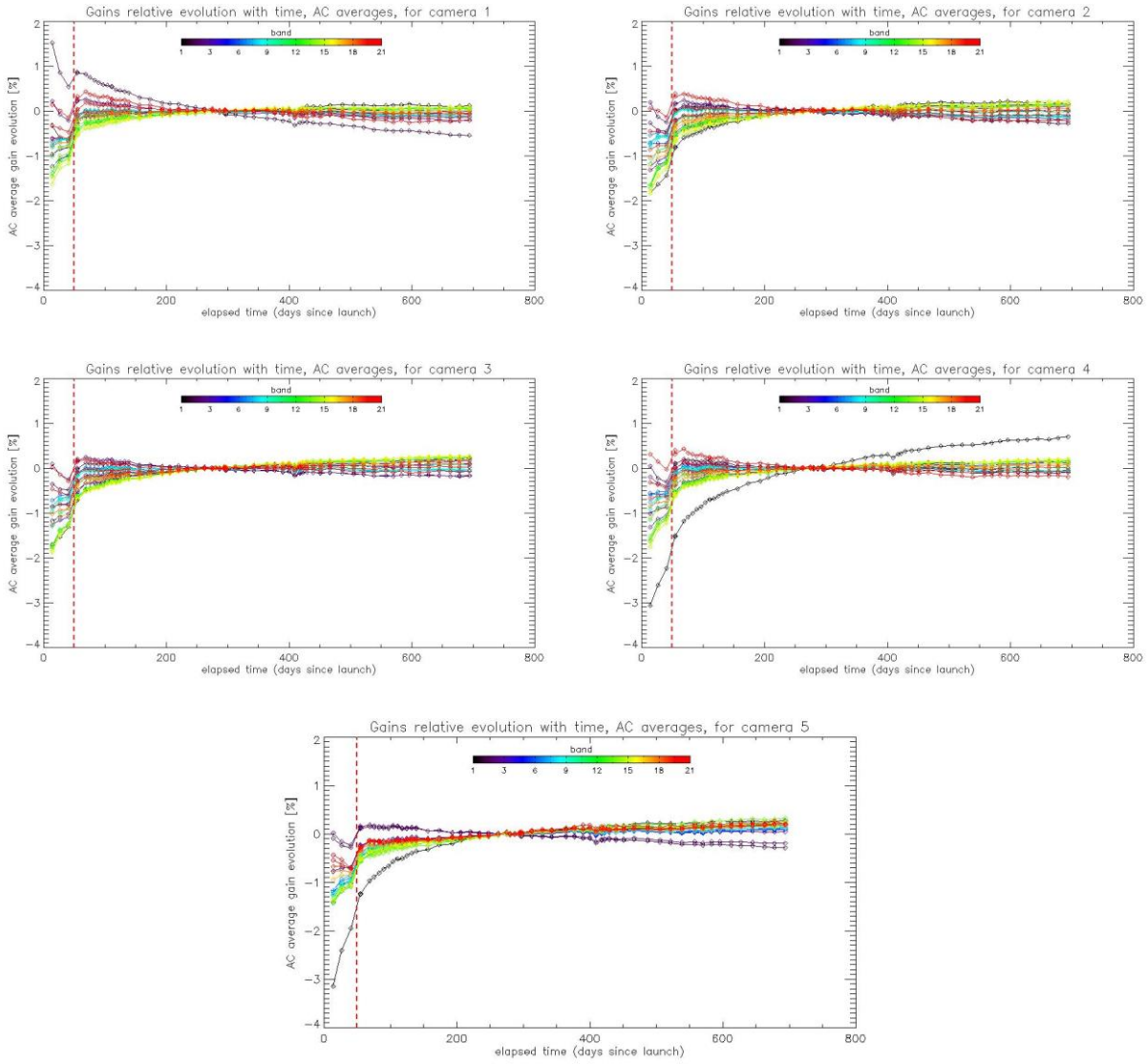

Figure 14: camera averaged gain relative evolution with respect to "best geometry" calibration (22/11/2016), as a function of elapsed time since launch; one curve for each band (see colour code on plots), one plot for each module. The star tracker anomaly fix (6/04/16) is represented by a vertical red dashed line.

The behaviour over the first two months of mission, really different and highlighted by Figure 14, is explained by the Star Tracker software anomaly during which the attitude information provided by the platform was corrupted, preventing to compute a correct illumination geometry, with a significant impact on the gain computation.

2.2.2.2 Instrument evolution modelling

As mentioned in cycle #22 Report, the OLCI Radiometric Model has been refreshed, and put in operations the 11/10/2017. The model has been derived on the basis of an extended Radiometric Calibration dataset (from 26/04/2016 to 27/08/2017), and includes the correction of the diffuser ageing for the five bluest bands (Oa1 to Oa5) for which it is clearly measurable. The model performance over

the complete dataset (including the 9 calibrations in extrapolation over about five months) remains better than 0.1% when averaged over the whole field of view (Figure 15) even if a small drift of the model with respect to most recent data is now visible. The previous model, trained on a Radiometric Dataset limited to 12/03/2017, shows a stronger drift of the model with respect to most recent data (Figure 16). Comparison of the two figures shows the improvement brought by the updated Model.

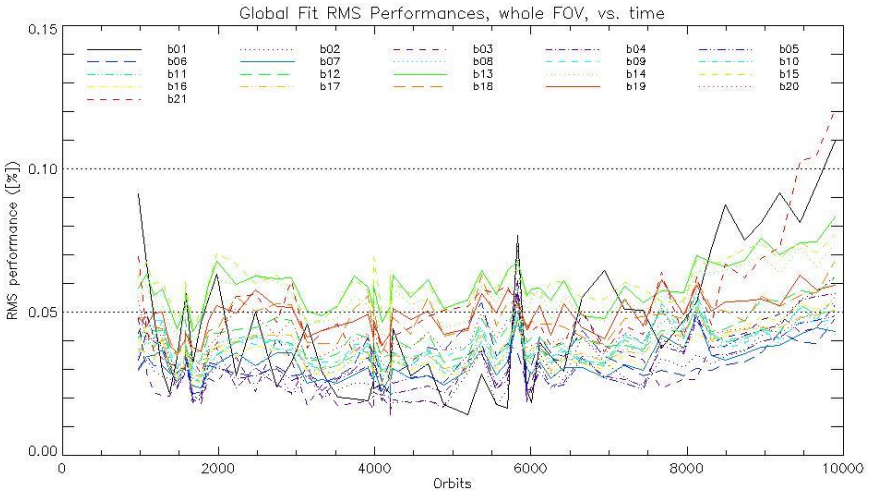

Figure 15: RMS performance of the Gain Model of current Processing Baseline as a function of orbit.

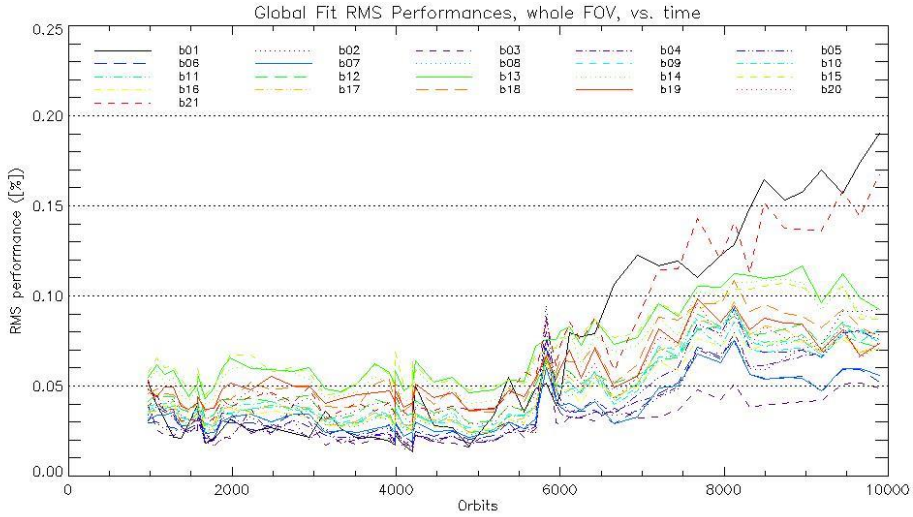

Figure 16: RMS performance of the Gain Model of previous Processing Baseline as a function of orbit.

The overall instrument evolution since channel programming change (25/04/2016) is shown on Figure 17.

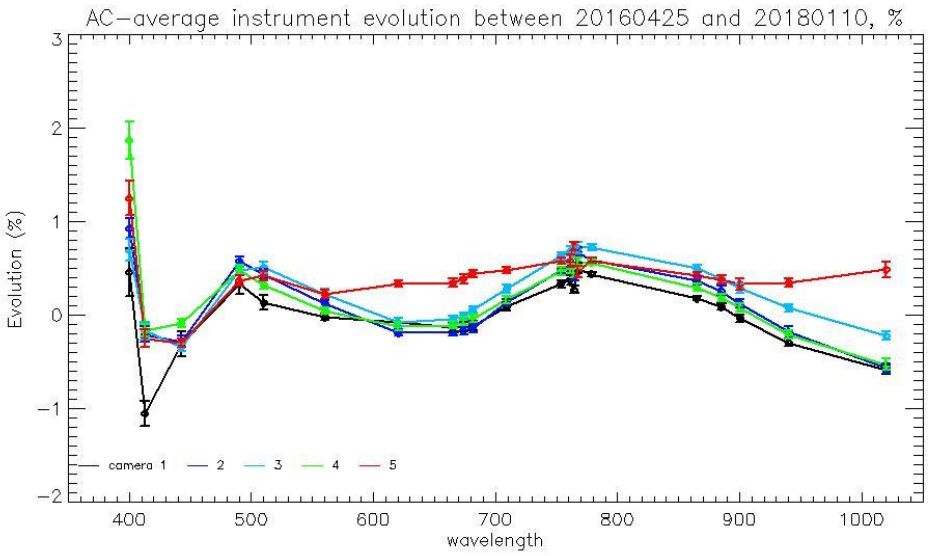

Figure 17: Camera-averaged instrument evolution since channel programming change (25/04/2016) and up to most recent calibration (10/01/2018) versus wavelength.

The overall per camera performance, as a function of wavelength, and at each orbit is shown on Figure 17 as the average and standard deviation of the model over data ratio.

Finally, Figure 19 to Figure 21 show the detail of the model performance, with across-track plots of the model over data ratios at each orbit, one plot for each channel.

Comparisons of Figure 17 to Figure 21 with their counterparts in Report of Cycle 22 clearly demonstrate the improvement brought by the new model whatever the level of detail.

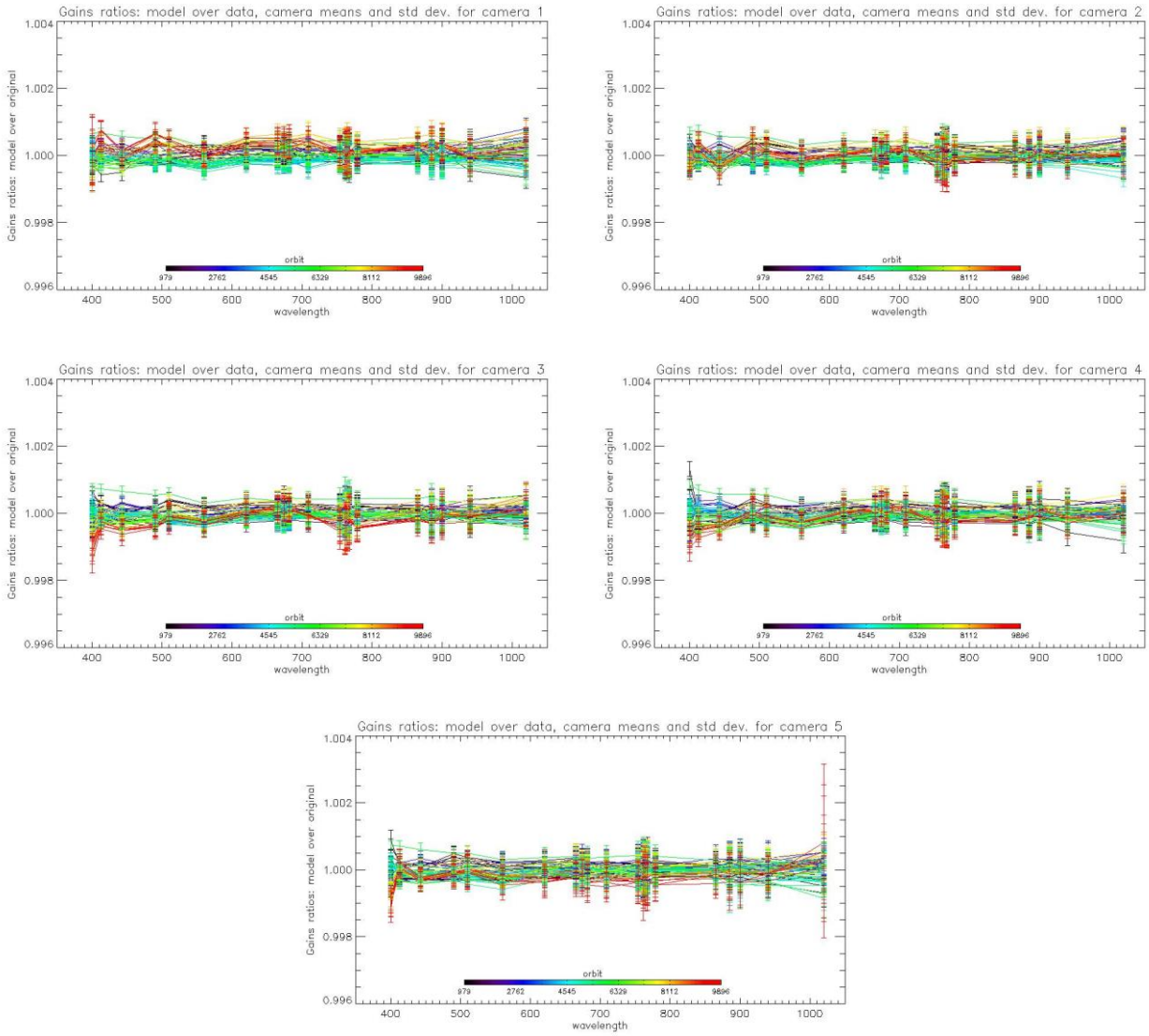

Figure 18: For the 5 cameras: Evolution model performance, as camera-average and standard deviation of ratio of Model over Data vs. wavelength, for each orbit of the test dataset, including 9 calibrations in extrapolation, with a colour code for each calibration from blue (oldest) to red (most recent).

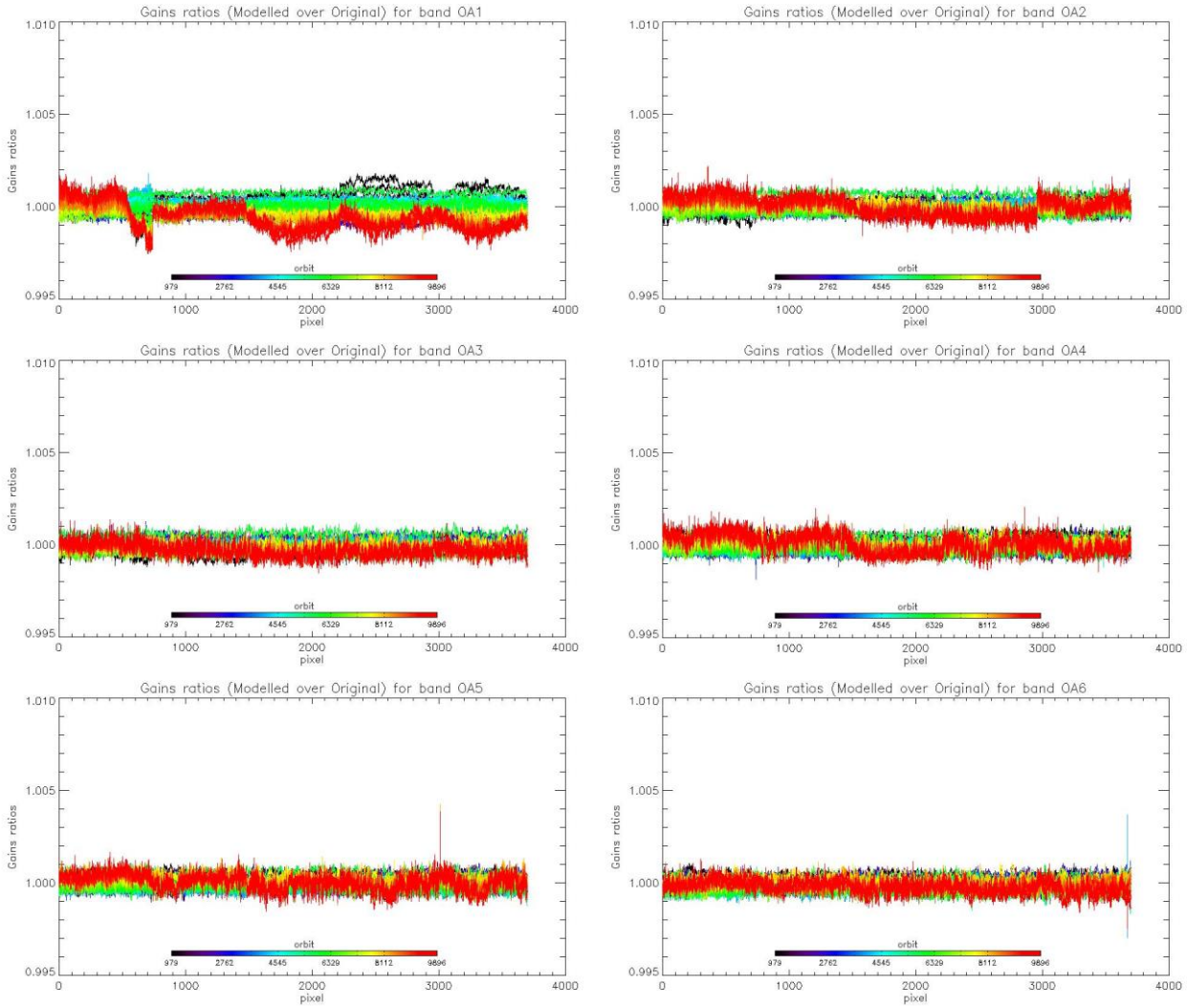

Figure 19: Evolution model performance, as ratio of Model over Data vs. pixels, all cameras side by side, over the whole current calibration dataset (since instrument programing update), including 9 calibrations in extrapolation, channels Oa1 to Oa6.

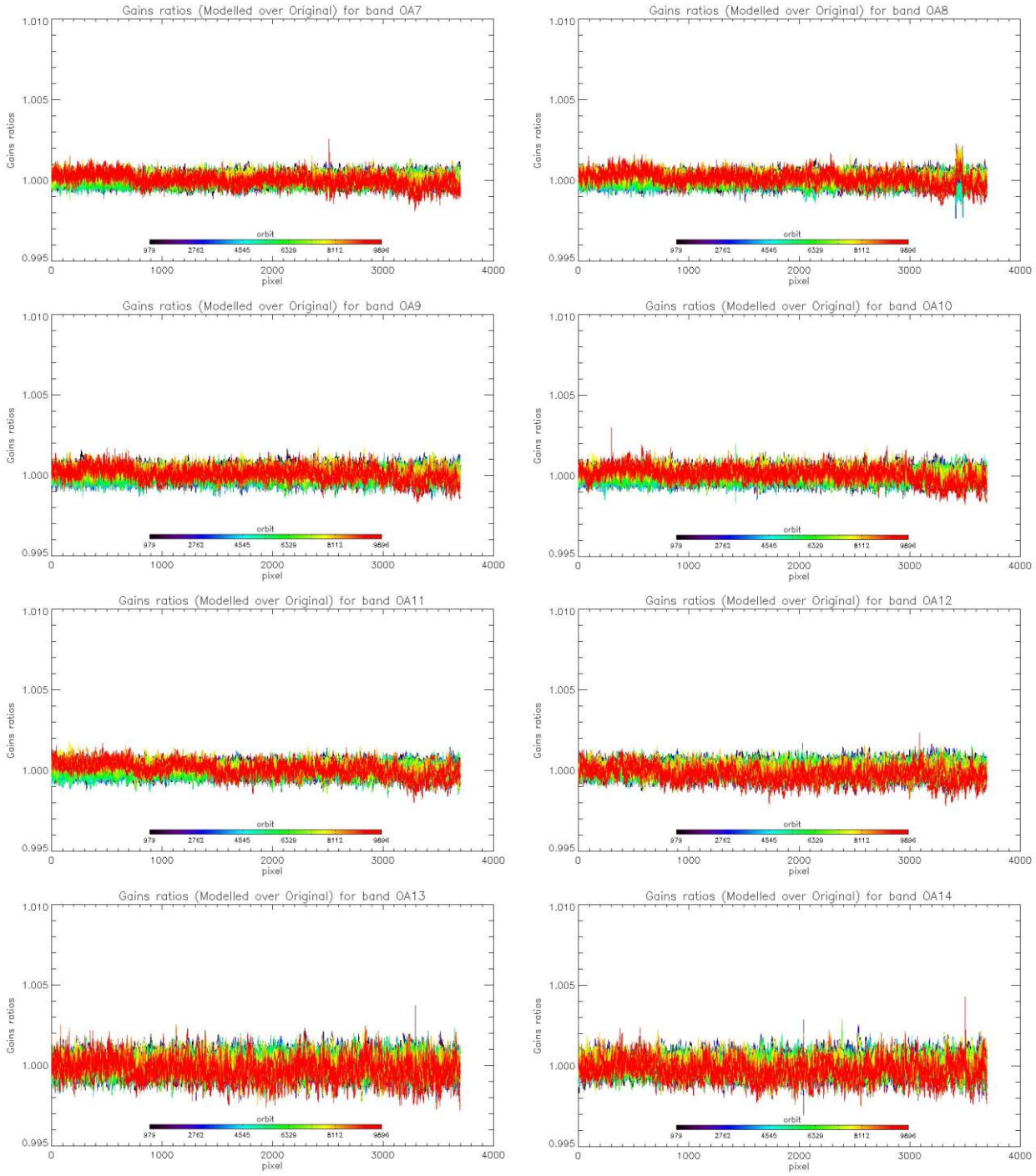

Figure 20: same as Figure 14 for channels Oa7 to Oa14.

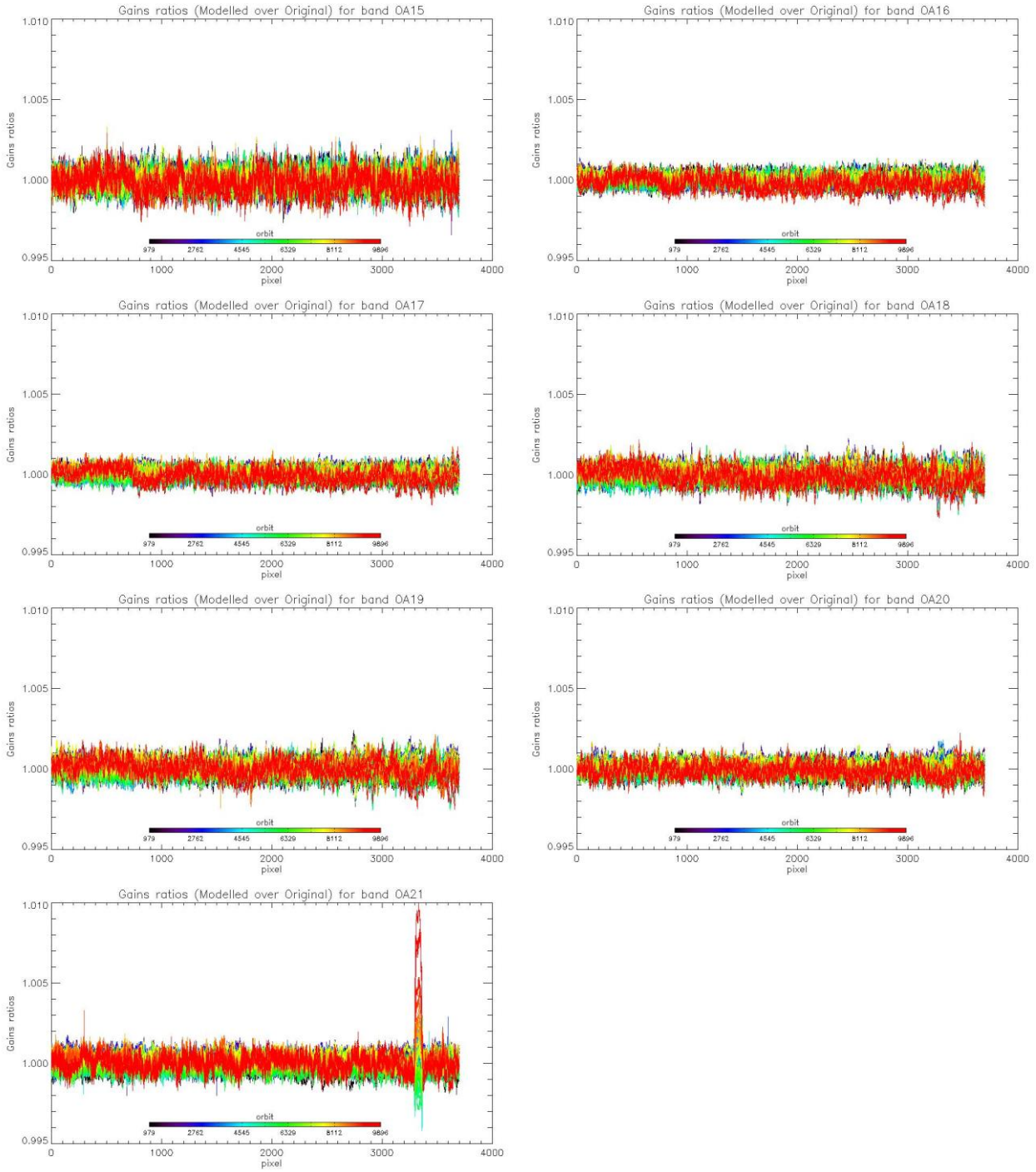

Figure 21: same as Figure 19 for channels Oa15 to Oa21.

2.2.3 Ageing of nominal diffuser [OLCI-L1B-CV-240]

There has been no calibration sequence S05 (reference diffuser) acquisition during cycle 026.

Consequently the last updated results (cycle 024) are still valid.

2.2.4 Updating of calibration ADF [OLCI-L1B-CV-260]

There has been no Calibration ADF generation during Cycle 26.

2.2.5 Radiometric Calibrations for sun azimuth angle dependency and Yaw Manoeuvres for Solar Diffuser on-orbit re-characterization [OLCI-L1B-CV-270 and OLCI-L1B-CV-280]

This activity has not evolved during cycle 026 and results presented in previous report are still valid.

2.3 Spectral Calibration [OLCI-L1B-CV-400]

There has been no Spectral Calibration acquisitions sequence during cycle 026.

Consequently, last results, presented in cycle 025 report are still valid.

2.4 Signal to Noise assessment [OLCI-L1B-CV-620]

2.4.1 SNR from Radiometric calibration data.

SNR computed for all calibration data as a function of band number is presented in Figure 22.

SNR computed for all calibration data as a function of orbit number for band Oa01 (the less stable band) is presented in Figure 23.

There is no significant evolution of this parameter during the current cycle and the ESA requirement is fulfilled for all bands.

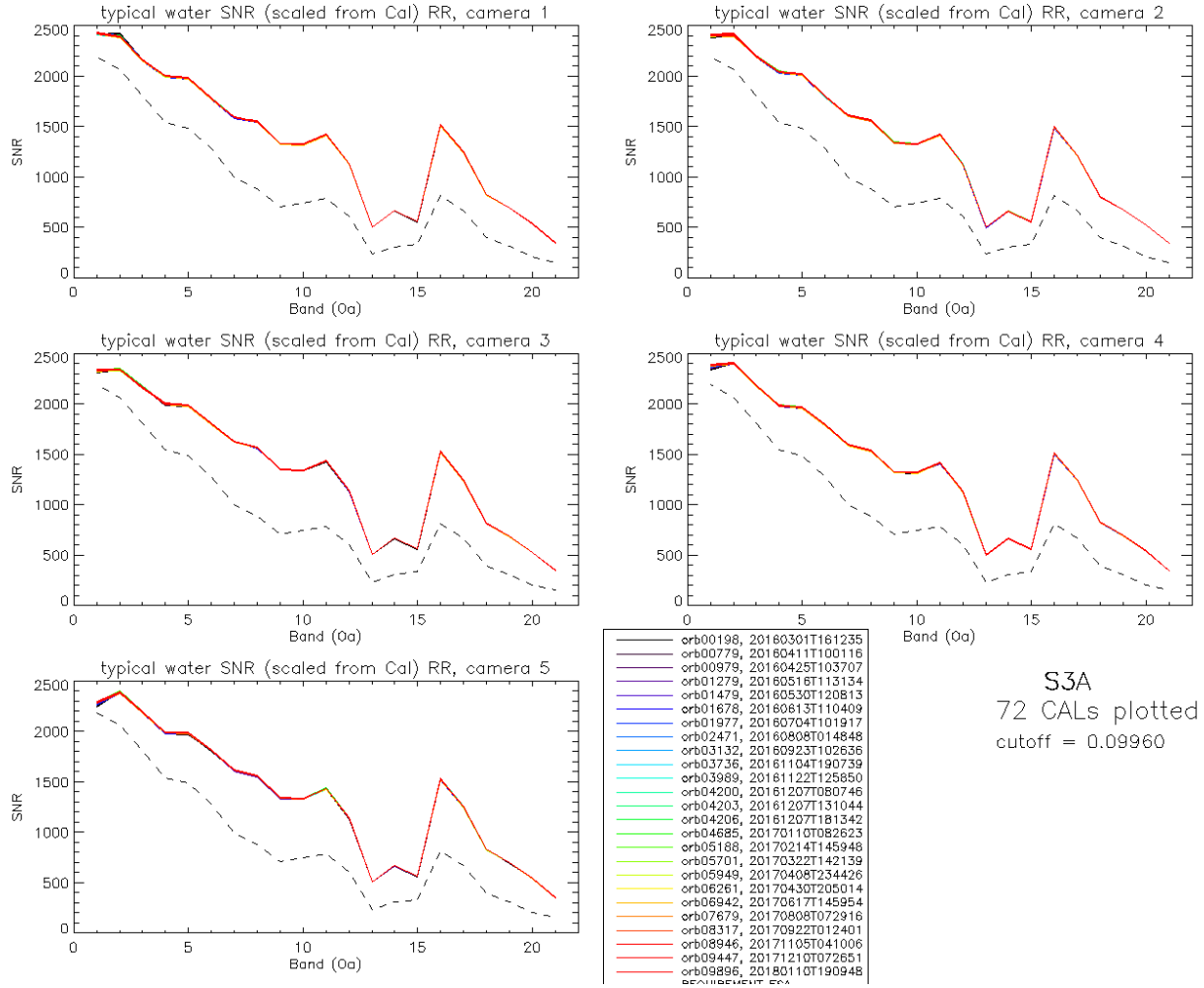

Figure 22: Signal to Noise ratio as a function of the spectral band for the 5 cameras. These results have been computed from radiometric calibration data. All calibrations except first one (orbit 183) are presents with the colours corresponding to the orbit number (see legend). The SNR is very stable with time: the curves for all orbits are almost superimposed. The dashed curve is the ESA requirement.

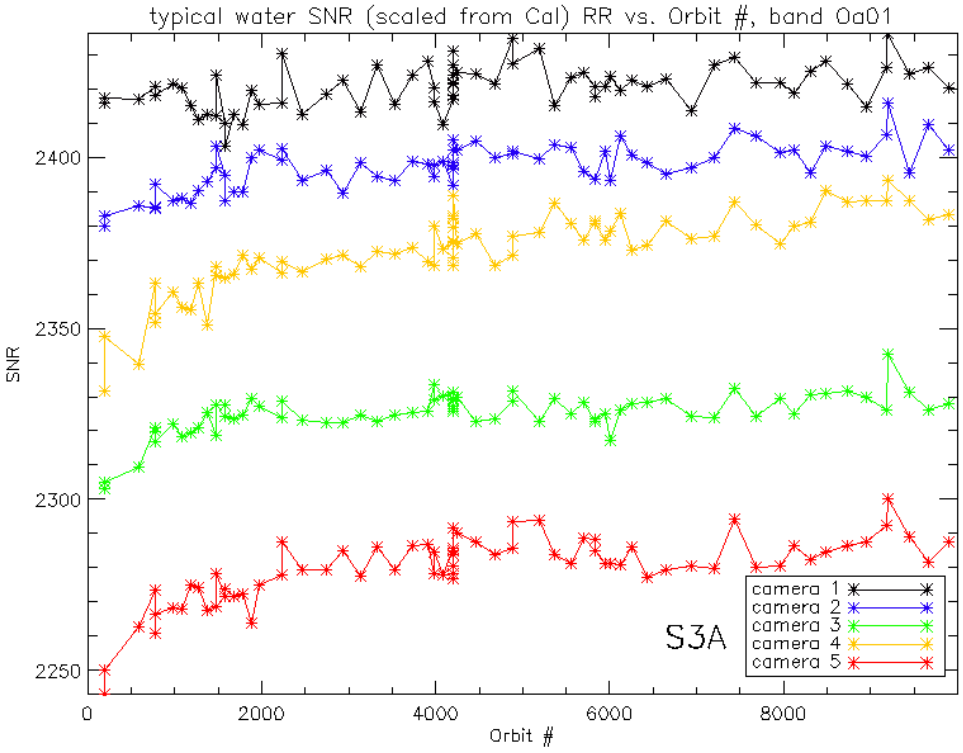

Figure 23: long-term stability of the SNR estimates from Calibration data, example of channel Oa1.

The mission averaged SNR figures are provided in Table 1 below, together with their radiance reference level. According to the OLCI SNR requirements, these figures are valid at these radiance levels and at Reduced Resolution (RR, 1.2 km). They can be scaled to other radiance levels assuming shot noise (CCD sensor noise) is the dominating term, i.e. radiometric noise can be considered Gaussian with its standard deviation varying as the square root of the signal; in other words: $SNR(L) = SNR(L_{ref}) \cdot \sqrt{\frac{L}{L_{ref}}}$. Following the same assumption, values at Full Resolution (300m) can be derived from RR ones as 4 times smaller.

Table 1: SNR figures as derived from Radiometric Calibration data. Figures are given for each camera (time average and standard deviation), and for the whole instrument. The requirement and its reference radiance level are recalled (in $mW.sr^{-1}.m^{-2}.nm^{-1}$).

□	L_{ref}	SNR	C1		C2		C3		C4		C5		All	
nm	LU	RQT	avg	*std*	avg	*std*	avg	*std*	avg	*std*	avg	*std*	avg	*std*
400.000	63.0	2188	2420	6.2	2397	6.7	2325	6.0	2372	11.6	2280	9.7	2359	6.9
412.000	74.1	2061	2395	7.5	2409	5.5	2340	4.8	2402	4.4	2386	6.7	2386	3.8
442.000	65.6	1811	2161	5.2	2199	5.6	2166	4.7	2185	4.1	2197	4.7	2182	3.3
490.000	51.2	1541	2000	5.1	2036	5.4	1996	3.8	1981	4.1	1988	5.0	2000	3.5
510.000	44.4	1488	1979	5.4	2013	5.0	1983	4.8	1966	4.7	1984	4.9	1985	4.0
560.000	31.5	1280	1776	4.4	1801	4.2	1801	4.7	1794	4.1	1818	3.6	1798	3.2
620.000	21.1	997	1591	4.2	1610	4.2	1625	3.2	1593	3.4	1615	3.6	1607	2.7
665.000	16.4	883	1546	4.7	1558	4.2	1566	3.9	1533	4.0	1560	3.8	1553	3.2
674.000	15.7	707	1329	3.3	1338	3.8	1350	2.9	1324	2.9	1341	3.9	1336	2.5
681.000	15.1	745	1320	3.7	1327	3.1	1337	2.8	1314	2.6	1332	3.8	1326	2.3
709.000	12.7	785	1420	4.7	1420	4.3	1434	3.5	1413	3.7	1429	3.1	1424	3.1
754.000	10.3	605	1127	3.4	1120	3.1	1134	3.6	1124	2.6	1138	3.1	1128	2.6
761.000	6.1	232	502	1.3	498	1.3	505	1.3	500	1.1	507	1.5	502	1.0
764.000	7.1	305	662	1.7	657	1.5	667	2.2	661	1.7	669	2.1	663	1.5
768.000	7.6	330	558	1.7	554	1.3	562	1.3	556	1.6	564	1.3	559	1.2
779.000	9.2	812	1514	5.2	1496	5.1	1523	5.5	1509	5.5	1525	5.2	1514	4.7
865.000	6.2	666	1243	3.8	1213	4.3	1238	4.3	1246	3.9	1250	2.9	1238	3.3
885.000	6.0	395	823	1.9	801	1.7	814	2.1	824	1.6	831	1.8	818	1.3
900.000	4.7	308	691	1.5	673	1.3	683	1.7	693	1.5	698	1.5	687	1.1
940.000	2.4	203	534	1.1	522	1.1	525	1.1	539	1.2	542	1.3	532	0.8
1020.000	3.9	152	345	0.8	337	0.7	348	0.8	345	0.7	351	0.7	345	0.5

2.4.2 SNR from EO data.

There has been no update on SNR assessment from EO data during the cycle. Last figures (cycle 9) are considered valid.

2.5 Geometric Calibration/Validation

Regular monitoring using the GeoCal Tool implemented within the MPMF continues. Late August results confirm good performance. Monitoring of the geolocation performance by correlation with GCP imagettes using the GeoCal tool over the period confirms that OLCI is compliant with its requirement: the centroid of the geolocation error is around 0.25 to 0.35 pixel in both along-track and across-track directions (Figure 24 & Figure 25). Completion of the time series (started using the partial reprocessing

dedicated to validation: 4 days every month between 26/04/16 and 12/03/2017) confirms the slow AL trend (Figure 26), the very last point, unless confirmed later on, is so far considered as an outlier.

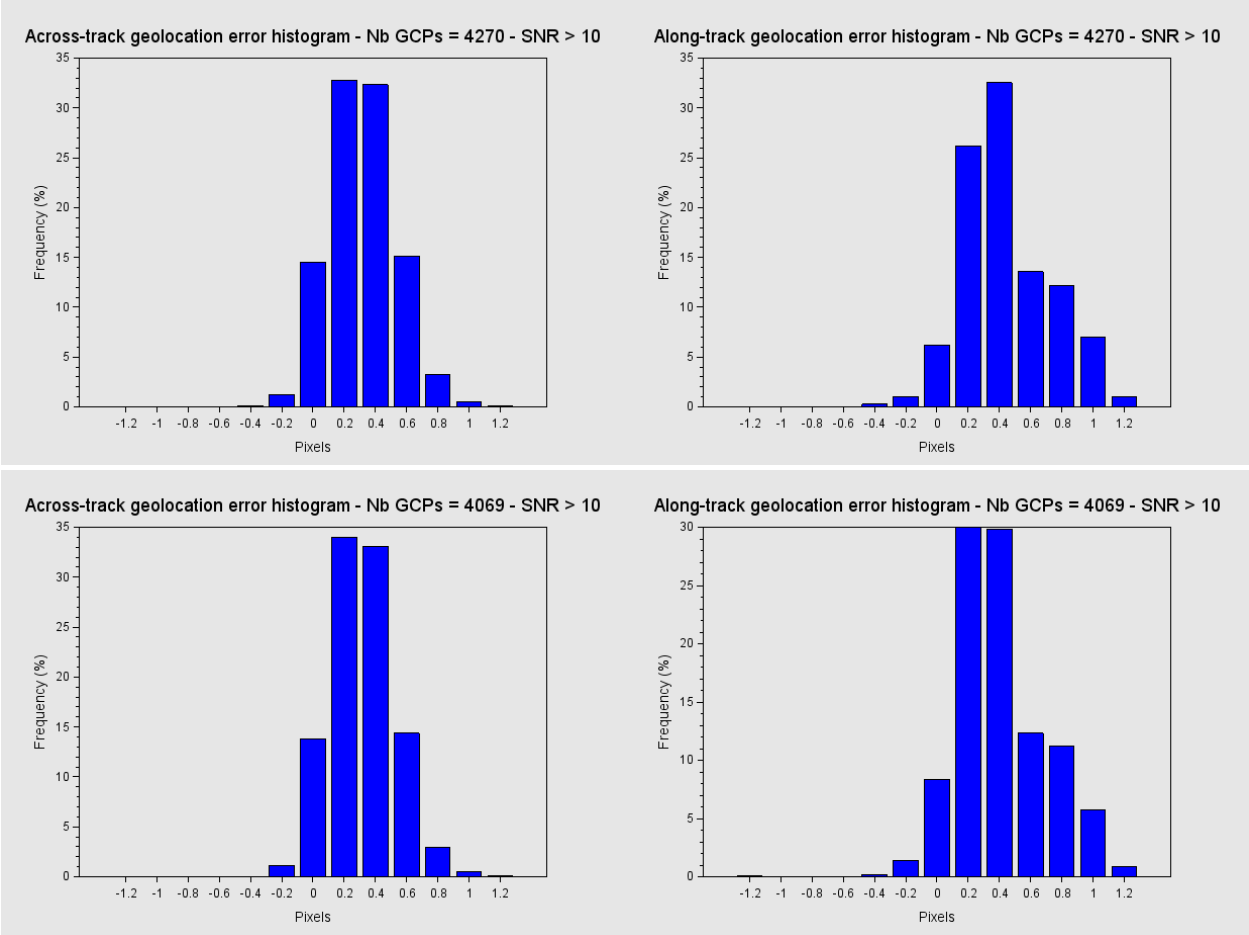

Figure 24: histograms of geolocation errors for the along-track (left) and across-track (right) directions, examples of 22/12/2017 (top) and 15/01/2018 (bottom).

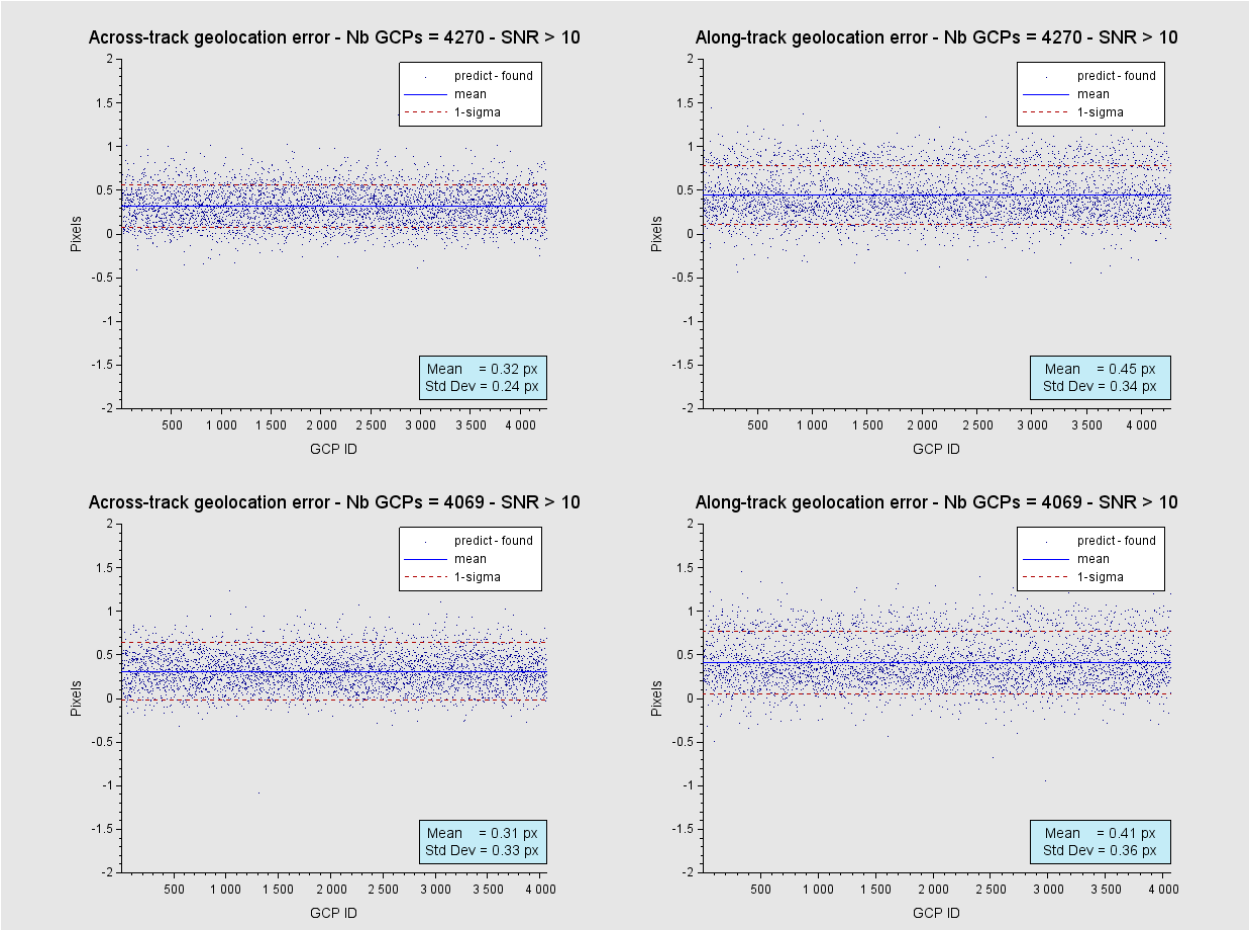

Figure 25: georeferencing error in along-track (left) and across-track (right) directions for all the GCPs, examples of 22/12/2017 (top) and 15/01/2018 (bottom).

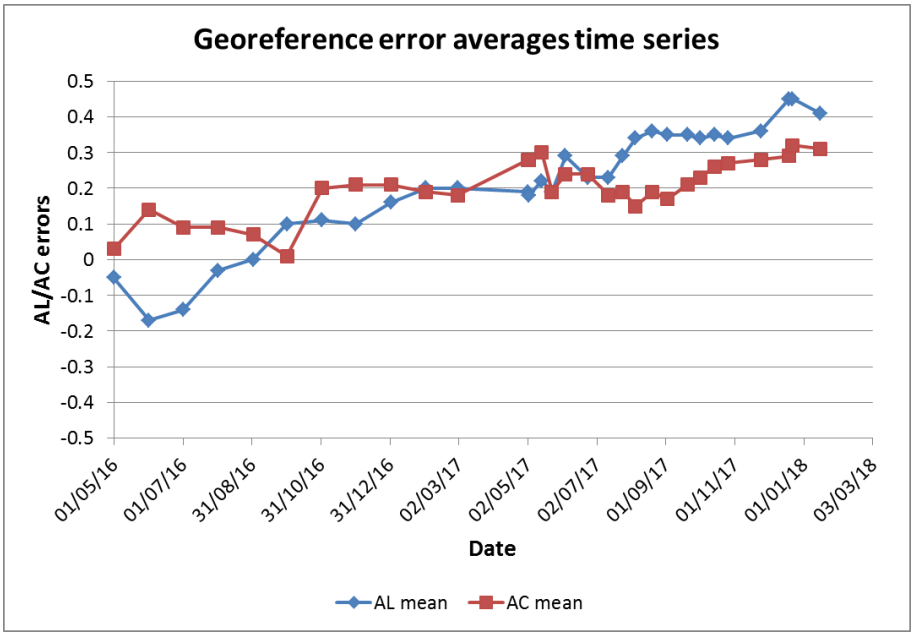

Figure 26: time series of geolocation errors for the along-track (blue) and across-track (red) directions over 18.7 months.

Per camera analysis has shown pointed out a significant drift of camera 3, yielding to non-compliance of that camera. An updated set of Geometric Calibration Models trained on data from the second half of 2017 has been delivered by ESTEC mid-December and has been validated by the S3-MPC. Results of this validation are shown on Figure 27 (left) as residuals of GCPs geolocation errors. Figure 27 (right) shows the same for the equivalent data set processed with the current Processing Baseline. The improvement is clear and further highlighted by the statistics given in Table 2 (reprocessed data) and Table 3 (current baseline). An example of geolocation performance time series (averages and standard deviations) is also shown on Figure 28 for Camera 3, highlighting the very good stability.

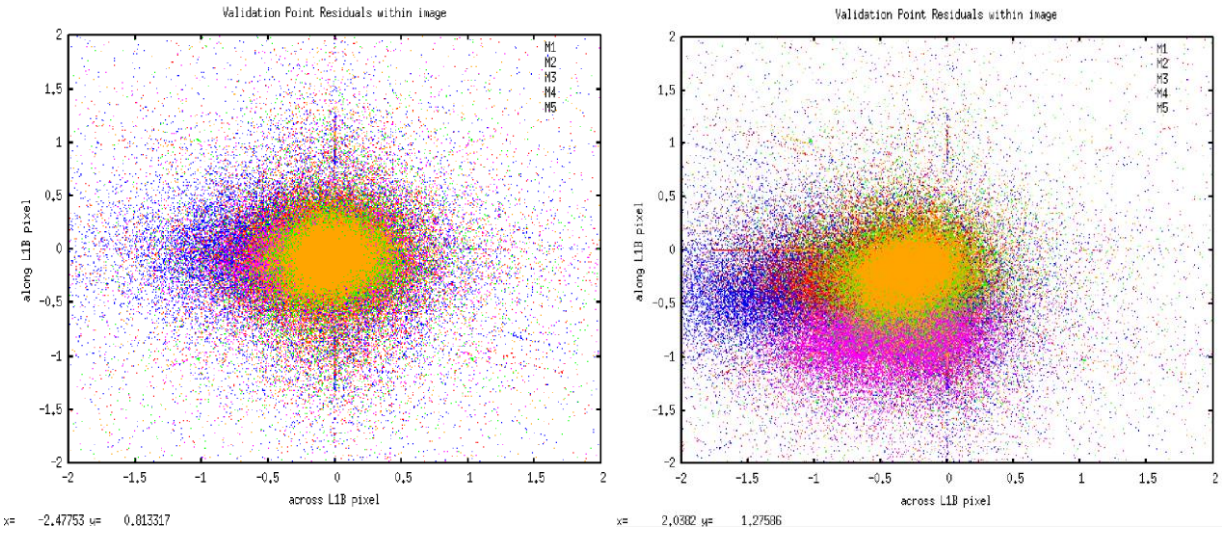

Figure 27: validation of the updated Geometric Calibration Models: residual geolocation error using new models (left) compared to those using current baseline on same data set. The validation data set extends from 15/10 to 29/11/2017, i.e. outside the ESTEC training set.

Table 2: validation of the updated Geometric Calibration Models: residual geolocation error statistics using reprocessed data.

Camera	biasAcross	biasAlong	sigmaAcross	sigmaAlong
1	-0.135143	-0.043965	0.004293	0.005967
2	-0.060582	-0.050120	0.005072	0.006990
3	-0.047512	-0.062590	0.005707	0.007773
4	-0.024701	-0.059935	0.005941	0.008315
5	-0.034563	-0.065549	0.005800	0.008051
RMS	0.072105	0.057011	0.005397	0.007468
Abs. RMS bias = 0.091921				

Table 3: validation of the updated Geometric Calibration Models: residual geolocation error statistics using current baseline data.

Camera	biasAcross	biasAlong	sigmaAcross	sigmaAlong
1	-0.508307	-0.382777	0.004245	0.005781
2	-0.417185	-0.274206	0.005023	0.006684
3	-0.357014	-0.767102	0.005626	0.007451
4	-0.315060	-0.232083	0.005872	0.007952
5	-0.294829	-0.196981	0.005738	0.007775
RMS	0.386281	0.424927	0.005335	0.007174
Abs. RMS bias = 0.574261				

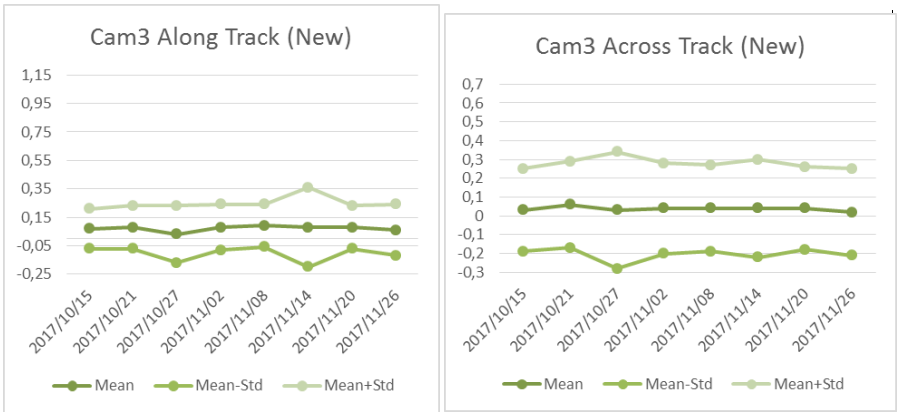

Figure 28: time series f along-track (left) and across-track (right) geolocation performance on the reprocessed data set. Central curves are the RMS performance while upper and lower ones are RMS ±1 standard deviation.

3 OLCI Level 1 Product validation

3.1 [OLCI-L1B-CV-300], [OLCI-L1B-CV-310] – Radiometric Validation

3.1.1 S3ETRAC Service

Activities done

The S3ETRAC service extracts OLCI L1 RR and SLSTR L1 RBT data and computes associated statistics over 49 sites corresponding to different surface types (desert, snow, ocean maximizing Rayleigh signal, ocean maximizing sunglint scattering and deep convective clouds). The S3ETRAC products are used for the assessment and monitoring of the L1 radiometry (optical channels) by the ESLs.

All details about the S3ETRAC/OLCI and S3ETRAC/SLSTR statistics are provided on the S3ETRAC website http://s3etrac.acri.fr/index.php?action=generalstatistics

- Number of OLCI products processed by the S3ETRAC service
- Statistics per type of target (DESERT, SNOW, RAYLEIGH, SUNGLINT and DCC)
- Statistics per sites
- Statistics on the number of records

For illustration, we provide below statistics on the number of S3ETRAC/OLCI records generated per type of targets (DESERT, SNOW, RAYLEIGH, SUNGLINT and DCC). Note that due to a technical issue, S3ETRAC production rate has been reduced in December and came back to nominal only recently. As a consequence, figures below do not represent the full production of December 2017.

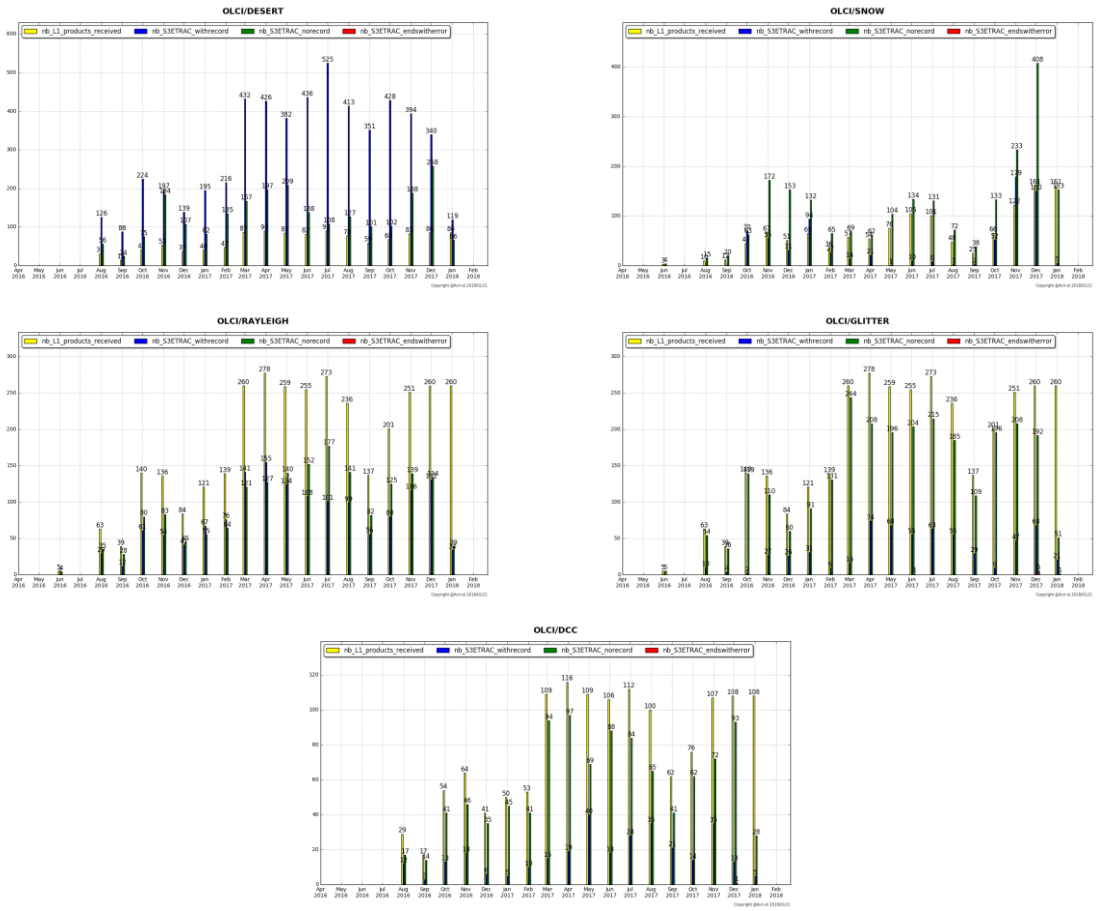

Figure 29: summary of S3ETRAC products generation for OLCI (number of OLCI L1 products Ingested, yellow – number of S3ETRAC extracted products generated, blue – number of S3ETRAC runs without generation of output product (data not meeting selection requirements), green – number of runs ending in error, red, one plot per site type).

3.1.2 Radiometric validation with DIMITRI

Highlights

- Run Rayleigh and Desert methods over the available products until 30th December 2017.
- About 116 new products from Cycle-25 are used in this analysis. The results (Rayleigh, Glint and PICS) are consistent with the previous cycle over the used CalVal sites.
- Good stability of the sensor could be observed, nevertheless, the time-series average shows higher reflectance over the VNIR spectral range with biases of 2%-4% except bands Oa06-Oa09
- Bands with high gaseous absorption are excluded.
- The results over PICS, Rayleigh and Glint methods from the reprocessed products **(REP006: July 2016-July 2017; December 2017 for PICS)** over 12 CalVal sites are analysed, and seem to be consistent with the results of the current processing baseline (PB:2.23)..

I-Validation over PICS

1. Downloading and ingestion of all the available L1B-LN1-NT products in the S3A-Opt database over the 6 desert CalVal-sites (Algeria3 & 5, Libya 1 & 4 and Mauritania 1 & 2) has been performed until 30th December 2017.

2. The results are consistent overall the six used PICS sites (Figure 30). OLCI reflectance shows a good stability over the analyzed period.

3. The temporal average over the period **April 2016 –** December **2017** of the elementary ratios (observed reflectance to the simulated one) shows values higher than 2% (mission requirements) over all the VNIR bands (Figure 31). The spectral bands with significant absorption from water vapour and O_2 (Oa11, Oa13 and Oa14) are excluded.

4. Algeria-3 site shows lower reflectance over the bands Oa17 (865 nm) than the other PICS since May 2017. This event is observed on Sentinel-2/MSI images too. It is most likely related to human/industrial activity in the area.

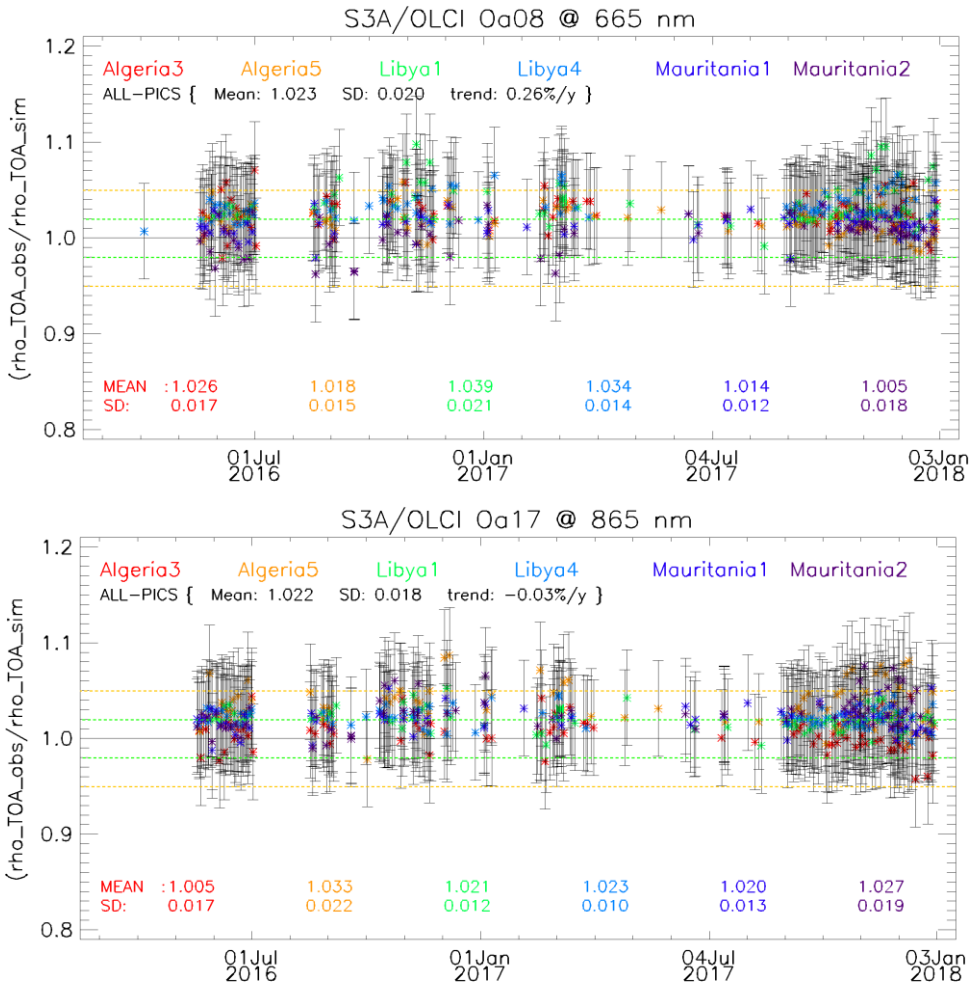

Figure 30: **Time-series of the elementary ratios (observed/simulated) signal from S3A/OLCI for (top to bottom) bands Oa03, Oa8 and Oa17 respectively over Six PICS Cal/Val sites. Dashed-green and orange lines indicate the 2% and 5% respectively. Error bars indicate the desert methodology uncertainty.**

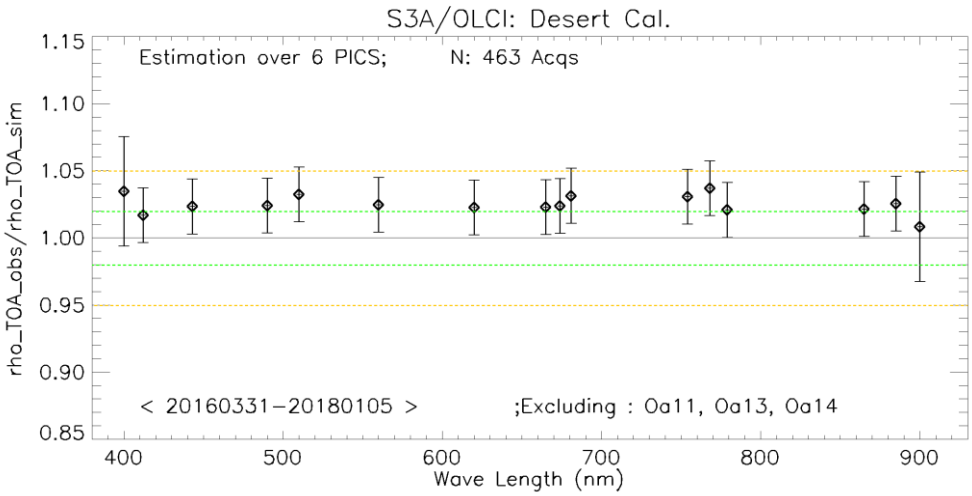

Figure 31: The estimated gain values for S3A/OLCI over the 6 PICS sites identified by CEOS over the period April 2016 – October 2017 as a function of wavelength. Dashed-green and orange lines indicate the 2% and 5% respectively. Error bars indicate the desert methodology uncertainty.

II-Intercomparison S3A/OLCI, S2A/MSI, LANDSAT/OLI and Aqua/MODIS over PICS

X-mission Intercomparison with MSI-A, OLI and MODIS-A is performed until December 2017. Figure 32 shows time-series of the elementary ratios from S2A/MSI, LANDSAT/OLI, Aqua/MODIS and S3A/OLCI over the LYBIA4 site over the period April-2016 until November -2017.

We observe a clear stability over the three sensors, associated with higher reflectance from OLCI wrt to MSI and MODISA. MODISA shows higher fluctuation wrt to MSI and OLCI ones.

Figure 33 shows the estimated gain over the different time-series from different sensors (MODISA, MSIA, OLCI and OLI) over PICS for the common bands with S2A/MSI. The spectral bands with significant absorption from water vapor and O_2 are excluded. OLCI-A seems to have higher gain (Figure 33) than the other sensors, which means that OLCI-A has higher reflectance that the ones simulated by PICS method.

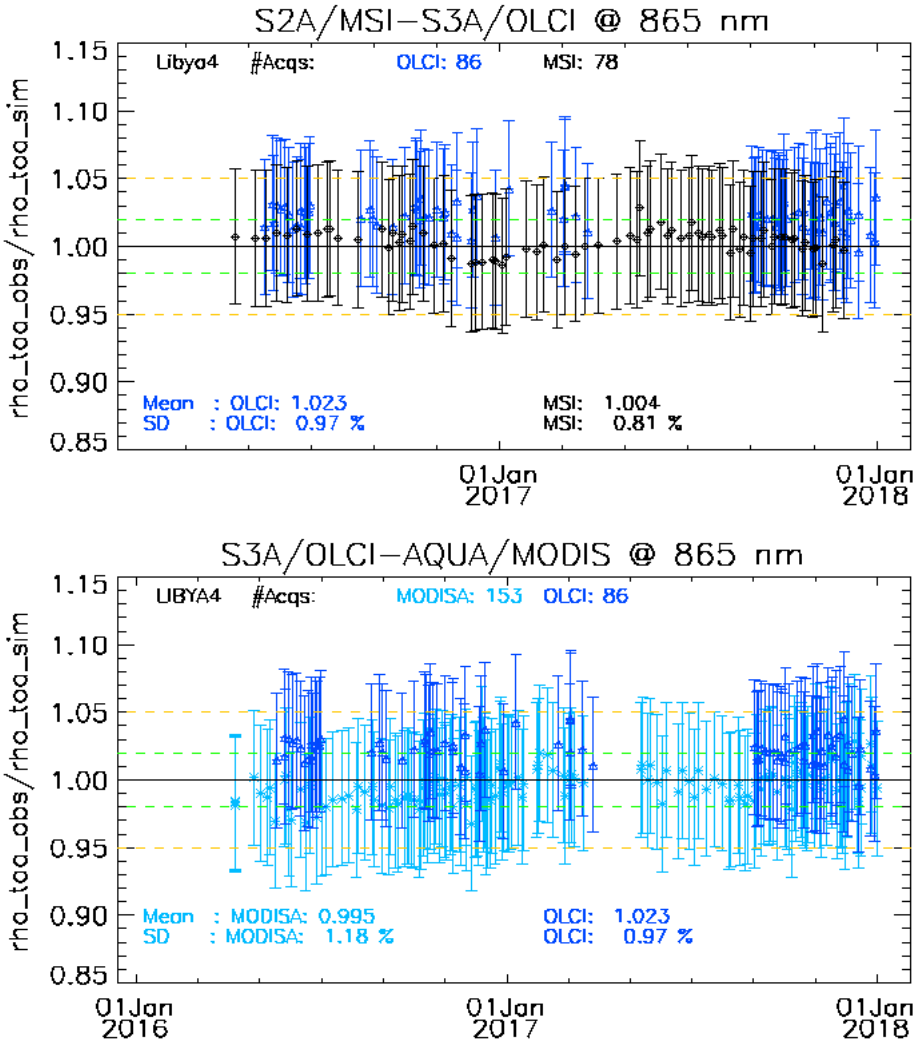

Figure 32: Time-series of the elementary ratios (observed/simulated) signal from (black) S2A/MSI, (blue) S3A/OLCI, and (Cyan) MODIS-A for band Oa17 (865nm) over the LIBYA4 site. Dashed-green and orange lines indicate the 2% and 5% respectively. Error bars indicate the desert methodology uncertainty.

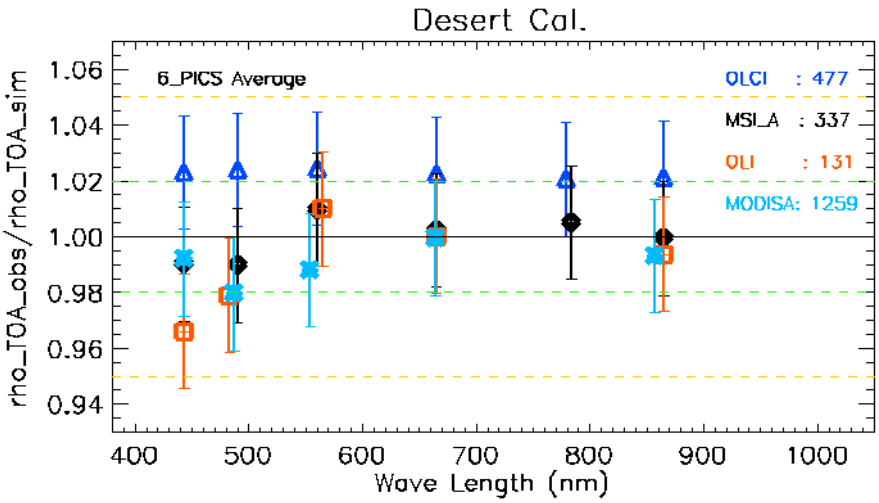

Figure 33: The estimated gain values (observed-signal /simulated-signal) averaged over different period (OLCI: 20160331-20180105; MSI-A: 20150701-20180105; MODIS-A: 20150101-20180101 and OLI: 20150701-20170330) over PICS as function of wavelength. The number of used-acquisitions from each sensor over the averaging period is indicated in the plot-legend.

III-Validation over Rayleigh

Rayleigh method has been performed over the available mini-files on the Opt-server until December 2017. The results produced with the configuration (ROI-AVERAGE) are consistent with the previous results of PICS method and from Cycles 24. While bands Oa01-Oa05 display a bias values between 2%-5%, bands Oa6-Oa9 exhibit biases within 2% (mission requirements) (Figure 34).

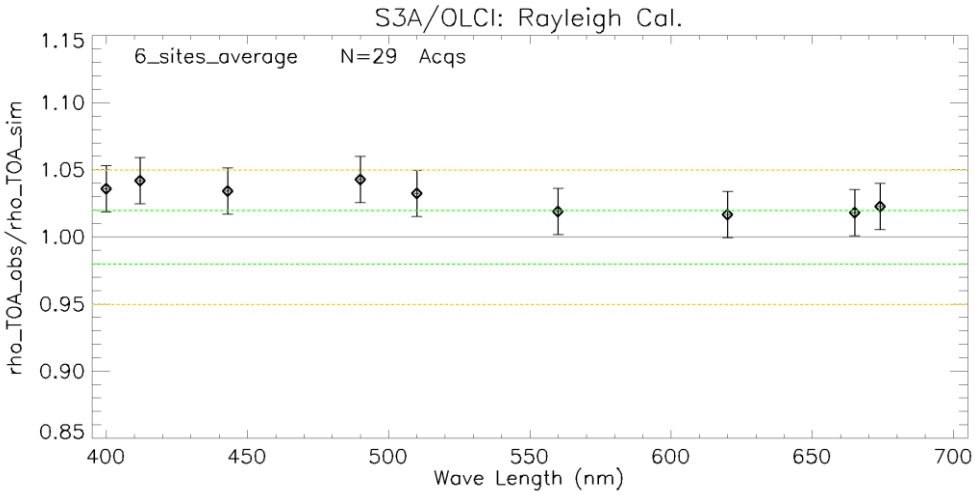

Figure 34: The estimated gain values for S3A/OLCI over the 6 Ocean CalVal sites (Atl-NW_Optimum, Atl-SW_Optimum, Pac-NE_Optimum, Pac-NW_Optimum, SPG_Optimum and SIO_Optimum) over the period December 2016 – December 2017 as a function of wavelength. Dashed-green, and orange lines indicate the 2%, 5% respectively. Error bars indicate the methodology uncertainty.

IV-Validation over Glint

Glint calibration method with the configuration (ROI-PIXEL) has been performed over the period December 2016 – end December 2017 from the available mini-files. The outcome of this analysis shows a good consistency with Rayleigh and the desert outputs over the NIR spectral range (see Figure 35).

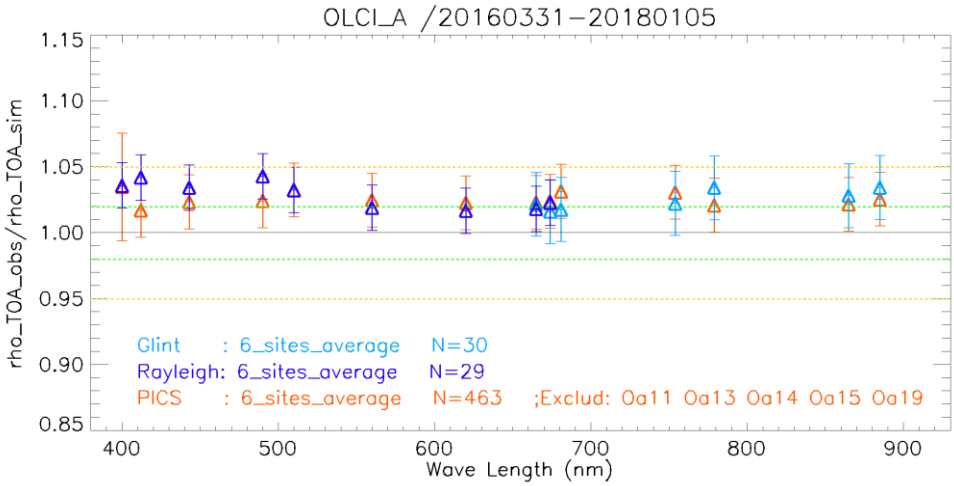

Figure 35: The estimated gain values for S3A/OLCI from Glint, Rayleigh and PICS over the period April 2016 – November 2017 for PICS and December 2016- December 2017 for Glint and December 2016-November 2017 for Rayleigh methods as a function of wavelength. We use the gain value of Oa8 from PICS method as reference gain for Glint. Dashed-green and orange lines indicate the 2% and 5% respectively. Error bars indicate the methods uncertainties.

V-Validation of the reprocessed products over ocean and desert sites from REP006

PICS, Rayleigh and Glint method have been performed over the available granules from the reprocessed products (REP006: July 2016 – July 2017; until Dec. 2017 for PICS) over the 6 PICS and 6 Ocean CalVal sites. Rayleigh results are produced with the configuration "ROI-AVERAGE" and Glint one with "ROI-PIXEL" configuration. While we observe a slightly higher values of Rayleigh gain coefficients wrt the results of the current processing baseline (PB:2.23)), PICS method results show a slightly lower gain coefficients but similar sensor stability (Figure 36). This could be related to the different averaging periods (Compare Figure 37 with Figure 35) however the differences are still within the methods error (~1%).

The outcome of this analysis shows a good consistency with the results of the current processing baseline (PB:2.23) over the VNIR spectral range (see Figure 37).

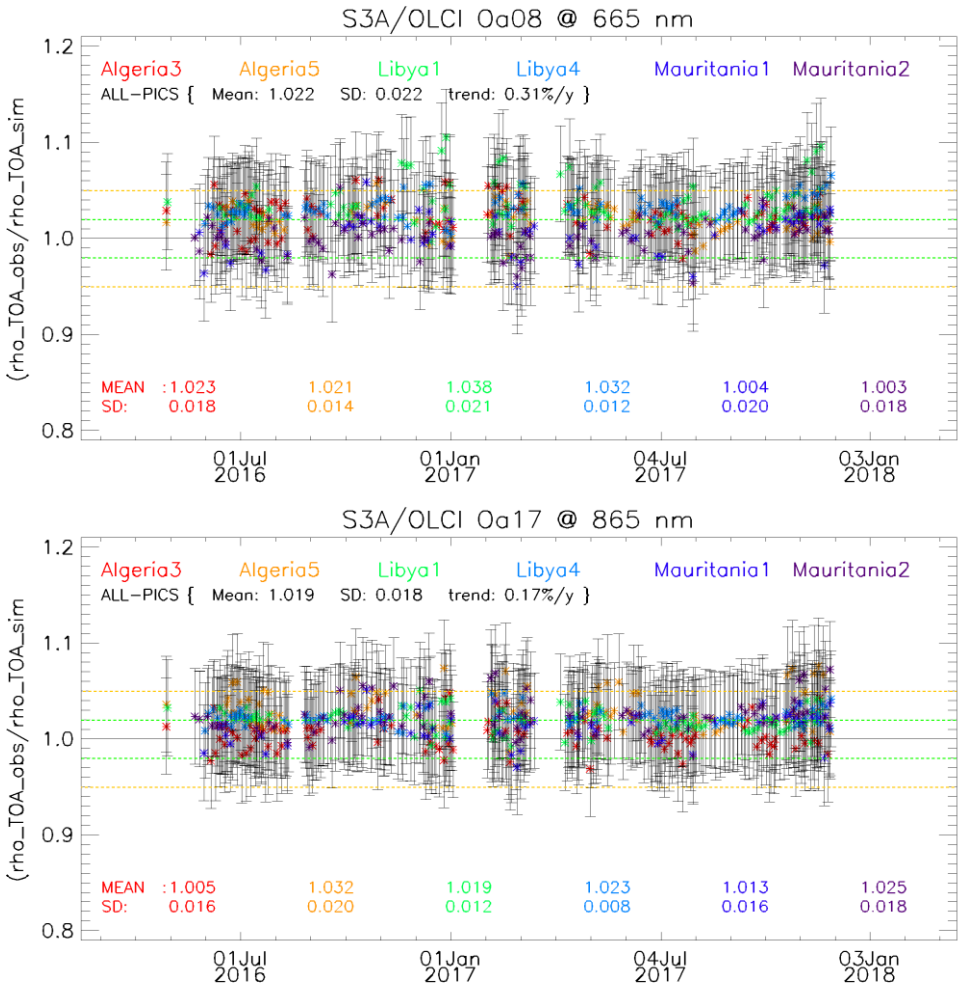

Figure 36: **Time-series of the elementary ratios (observed/simulated) signal from S3A/OLCI products (REP006: July 2016 – December 2017) for (top to bottom) bands Oa08 and Oa17 respectively over Six PICS Cal/Val sites. Dashed-green and orange lines indicate the 2% and 5% respectively. Error bars indicate the desert methodology uncertainty.**

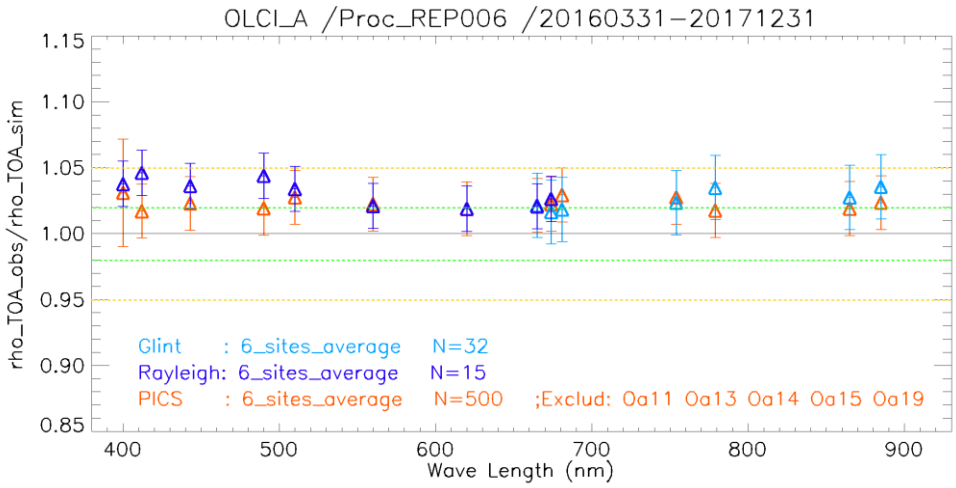

Figure 37: The estimated gain values for S3A/OLCI from PICS, Glint and Rayleigh methods over the reprocessed products (REP006: July 2016 – July 2017; Dec 2017 for PICS) as a function of wavelength. We use the gain value of Oa8 from Rayleigh method as reference gain for Glint. Dashed-green and orange lines indicate the 2% and 5% respectively. Error bars indicate the methods uncertainties.

3.1.3 Radiometric validation with OSCAR

There has been no new result during the cycle. Last figures (cycle 25) are considered valid.

3.2 [OLCI-L1B-CV-320] – Radiometric Validation with Level 3 products

There has been no new result during the cycle. Last figures (cycle 20) are considered valid.

4 Level 2 Land products validation

4.1 [OLCI-L2LRF-CV-300]

There has been no new result during the cycle. Last figures (cycle 25) are considered valid.

4.2 [OLCI-L2LRF-CV-410 & OLCI-L2LRF-CV-420] – Cloud Masking & Surface Classification for Land Products

There has been no update of the Cloud Masking & Surface Classification for Land Products during Cycle 026. Last figures (cycle 24) are considered valid.

5 Level 2 Water products validation

5.1 [OLCI-L2-CV-210, OLCI-L2-CV-220] – Vicarious calibration of the NIR and VIS bands

There has been no update of the SVC (System Vicarious Calibration) during Cycle 026. Last figures (cycle 17) are considered valid.

5.2 [OLCI-L2WLR-CV-300, OLCI-L2WLR-CV-310, OLCI-L2WLR-CV-32, OLCI-L2WLR-CV-330, OLCI-L2WLR-CV-340, OLCI-L2WLR-CV-350, OLCI-L2WLR-CV-360 and OLCI-L2WLR-CV-370] – Level 2 Water-leaving Reflectance product validation.

Activities done

- The focus for this time period has been on the rolling archive None Time Critical (NT) data from September 1st onward.
- All extractions and statistics have been regenerated from September 1st onward (rolling archive availability) for WFR data. The available matchups therefore cover the end of summer to winter situations. Time range available for last processing period covered September 1st to January 13th time period.
- No new matchup from AERONET-OC stations and MOBY are available for this time period due to delay in data retrieval.
- ARGANS did a specific study of Marine Reflectance validation from the reprocessed dataset over three AERONET-OC in-situ sites. Preliminary results are presented below in sub-section “Validation against in-situ data in the Baltic Sea and the Long Island Sound”.

Overall Water-leaving Reflectance performance

There has been no new result during the cycle (lack of in-situ data). Last figures (cycle 25) are considered valid. OLCI extractions over the Validation sites have processed nominally as show for example for MOBY on Figure 38. Performance figures over the whole available data set are recalled in Table 4.

Table 4: Statistics over the last reporting period (September 1st to November 26th), FR data.

lambda	N	RPD	|RPD|	MAD	RMSE	slope	intercept	r2
400	14	-9.9%	11.7%	-0.0049	0.0065	0.9241	-0.0012	0.5049
412	30	-4.3%	18.6%	-0.0030	0.0061	0.7920	0.0026	0.9417
443	38	-6.6%	15.4%	-0.0020	0.0039	0.8056	0.0017	0.9438
490	49	-4.0%	10.4%	-0.0008	0.0020	0.8235	0.0018	0.8666
510	14	-8.1%	10.8%	-0.0009	0.0015	2.5638	-0.0183	0.2207
560	47	-6.6%	16.2%	-0.0005	0.0015	0.9610	-0.0002	0.8234

Figure 38 below presents MOBY in situ and OLCI time series over the reprocessing period completed by current baseline. MOBY in situ data are not yet available for the December and January time period. On the in situ and overlap time period, a good agreement is observed.

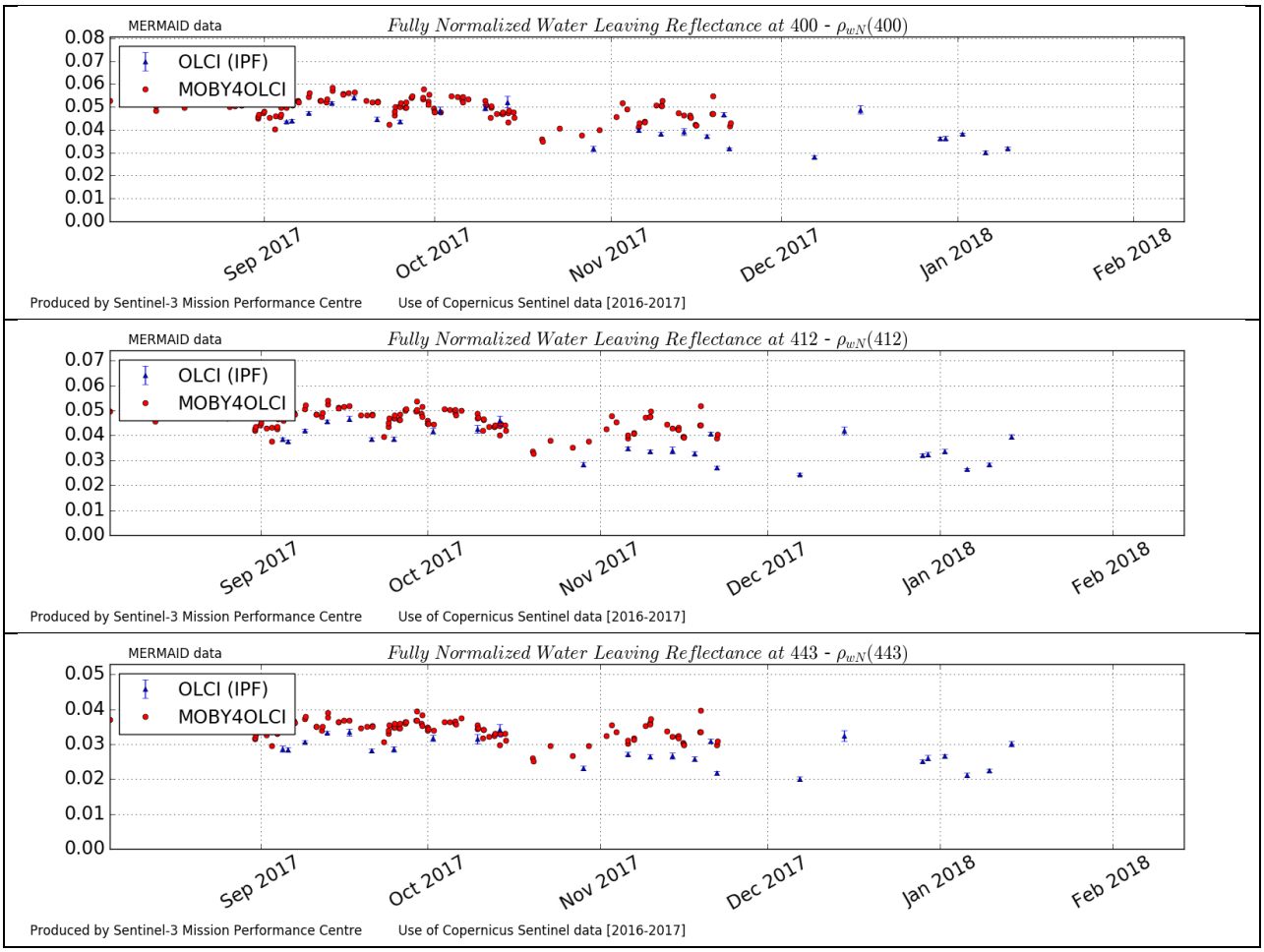

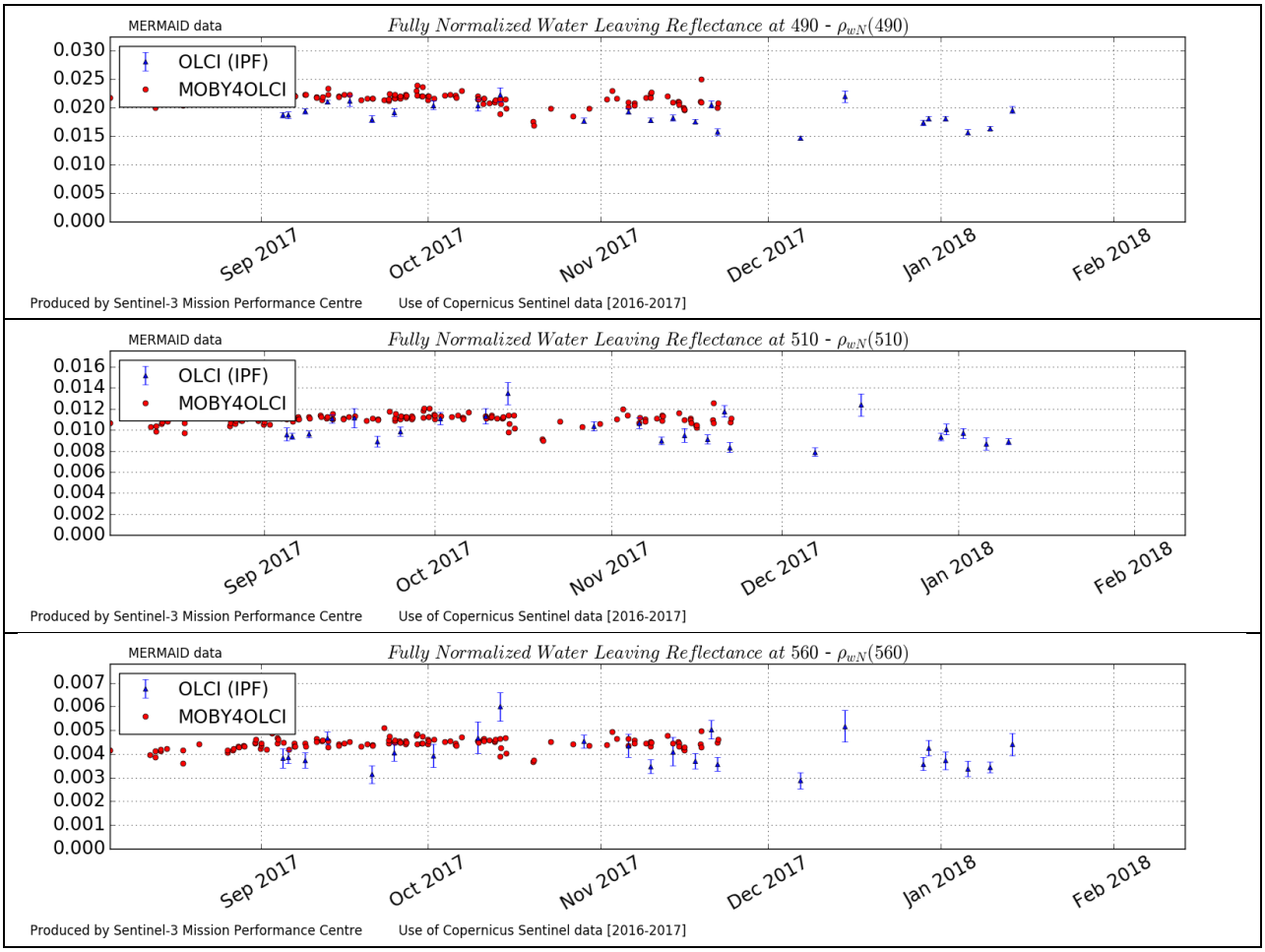

Figure 38: MOBY time series over current report period

Validation against in-situ data in the Baltic Sea and the Long Island Sound (NW-Atlantic ocean)

I-Used Datasets

S3A/OLCI L2-WFR products over the Baltic Sea and the Long Island Sound in 2017 were retrieved from the Copernicus Online Data Access web page (listed below).

OLCI data around GDLT site

- S3A_OL_2_WFR___20170713T095111_201713T095411_20170713T120404_0179_020_022_1980_MAR_O_NR_002.SEN3
- S3A_OL_2_WFR___20170731T084351_20170731T084651_20170731T124949_0179_020_278_1980_MAR_O_NR_002.SEN3
- S3A_OL_2_WFR___20170824T100224_20170824T100524_20170824T120733_0179_021_236_1980_MARO_NR_002.SEN3

OLCI data around HLT site

- S3A_OL_2_WFR___20170707T090618_20170707T090918_20170707T111250_0179_019_321_MAR_O_NR_002.SEN3
- S3A_OL_2_WFR___20170714T092500_20170714T092800_20170715T172655_0179_020_036_1979_MAR_O_NR_002.SEN3
- S3A_OL_2_WFR___20170727T084735_20170727T085035_20170727T105331_0179_020_221_1979_MAR_O_NR_002.SEN3
- S3A_OL_2_WFR___20170814T092115_20170814T092415_20170815T195055_0179_021_307_1908_MAR_O_NR_002.SEN3
- S3A_OL_2_WFR___20170923T084351_20170923T084651_20170923T104842_0179_022_278_1979_MAR_O_NR_002.SEN3

OLCI data around LISCO site

- S3A_OL_2_WFR____20170709T150353_20170709T150653_20170710T214245_0179_019_353_2340_MAR_O_NT_002.SEN3
- S3A_OL_2_WFR____20170801T150737_20170801T151037_20170802T225652_0179_020_296_2340_MAR_O_NT_002.SEN3
- S3A_OL_2_WFR____20170831T152704_20170831T153004_20170901T233357_0180_021_339_2159_MAR_O_NT_002.SEN3
- S3A_OL_2_WFR____20170904T152319_20170904T152619_20170904T172425_0179_022_011_2159_MAR_O_NR_002.SEN3
- S3A_OL_2_WFR____20170908T151935_20170908T152235_20170908T172109_0179_022_068_2160_MAR_O_NR_002.SEN3
- S3A_OL_2_WFR____20171028T152319_20171028T152619_20171029T220011_0179_024_011_2160_MAR_O_NT_002.SEN3
- S3A_OL_2_WFR____20171121T150053_20171121T150353_20171122T210241_0179_024_353_2159_MAR_O_NT_002.SEN3
- S3A_OL_2_WFR____20171128T151935_20171128T152235_20171128T171948_0179_025_068_2159_MAR_O_NR_002.SEN3

The AERONET-OC measurements from the following sites have been used:

- The Helsinki Lighthouse Tower (HLT), in the Gulf of Finland
- The Gustav Dalen Lighthouse Tower (GDLT), in the northern Baltic Proper.

The HLT, owned and managed by the Finnish Maritime Administration, is located in the Gulf of Finland (59.949° N, 24.926°), at approximately 12 nautical miles south-east of the harbour of Helsinki in an average water depth around 13 m.

GDLT, owned and managed by the Swedish Maritime Administration, is located in the northern Baltic Proper (58.594° N, 17.467° E) at approximately 10 nautical miles off the Swedish Coast and 5 nautical miles from the closest island with an average water depth around 16 m
The LISCO off-shore platform (40.95 ° N, 73.34 ° W), is located in the Long Island Sound near Northport, New York.

The sites and their surroundings are shown in Figure 39.

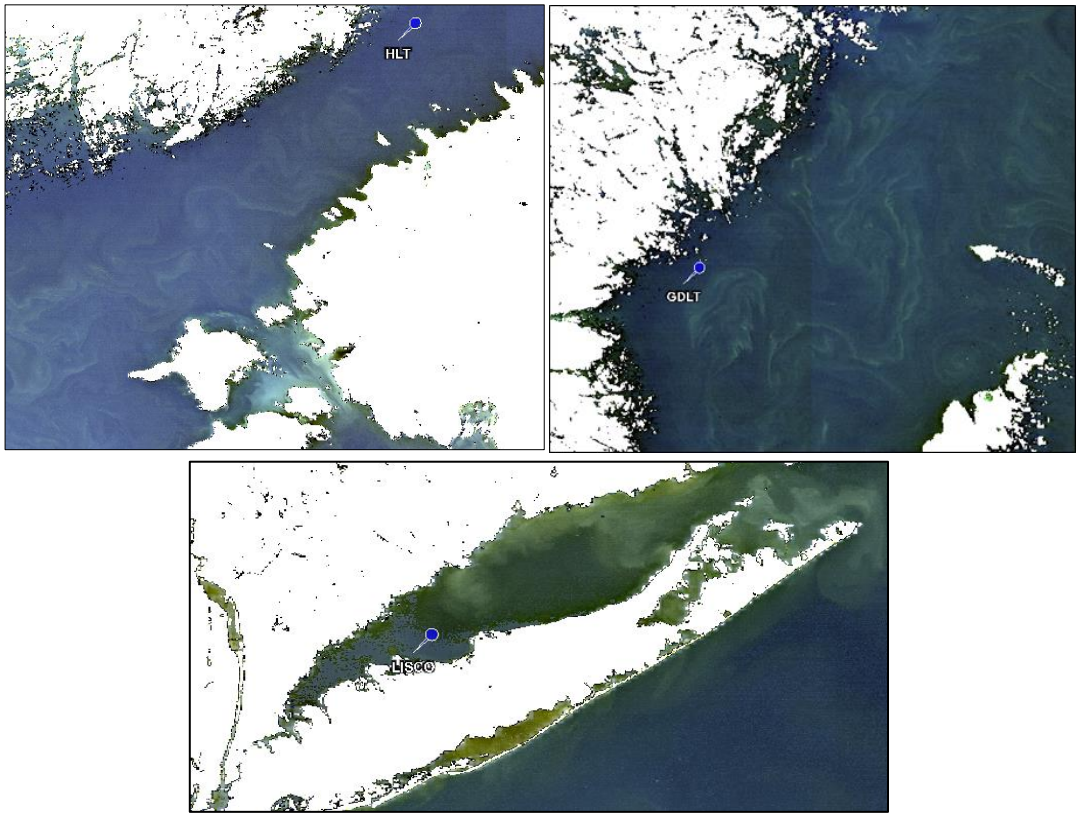

Figure 39: Location of the sites around the HLT (top left), the GDLT (top right) and the LISCO platform (bottom).

II-Methods

Comparisons were made using the OLCI L2-WFR products and AERONET-OC in-situ measurements for normalized water-leaving reflectance (ρ_{WN}). The selection of OLCI L2-WRF products were restricted to images showing clear skies and filtered for contamination. For each band, the normalized water-leaving reflectance was filtered using invalid retrieval flag RWNEG_*. The AERONET-OC level 1.5 measurements have been used in this report. The AERONET-OC measurements have been selected as the closest in time to Sentinel-3A overpasses. Regarding OLCI-L2-WFR products, macro-pixels are used as 9x9 pixels average over GDLT and HLT and 5x5 pixels for LISCO site.

For the matchup analysis, data products were evaluated through the scattering and |RDP|, the bias as absolute relative percent difference $|RDP| = \frac{1}{N}\sum^{N}\frac{|y-x|}{|x|}.100\%$

Where y_i is OLCI $\rho_{WN}(\lambda)$, x_i is the in-situ $\rho_w(\lambda)$, and N the number of samples.

III-Preliminary results

1) <u>Baltic Sea</u>

The normalized water reflectance (ρ_{WN}) from OLCI L2-WFR -averaged over the valid pixels from the 5 days - shows similar behaviors to the in-situ measurement of GDLT and HLT (Figure 40). The spectra and features are consistent with these of turbid coastal waters, and are similar to the values retrieved in

oceanic areas by [Zibordi et al 2009b, Melin & Vantrepotte 2015]. Those features have been associated with case-2 waters dominated by color dissolved organic matter (CDOM) and a low aerosol load of continental origin. The measurement for total suspended matter (TSM) around GDLT and HLT by OLCI, respectively in Tables 1 and 2, are consistent with a strong presence of CDOM. Those results, for areas both located in intracontinental shallow waters, with limited exchange with the North Sea and important discharge of material due to human activities are consistent with previous local studies from *[Darecki & Stramski 2004, Hojersley & Aas 2001]*.

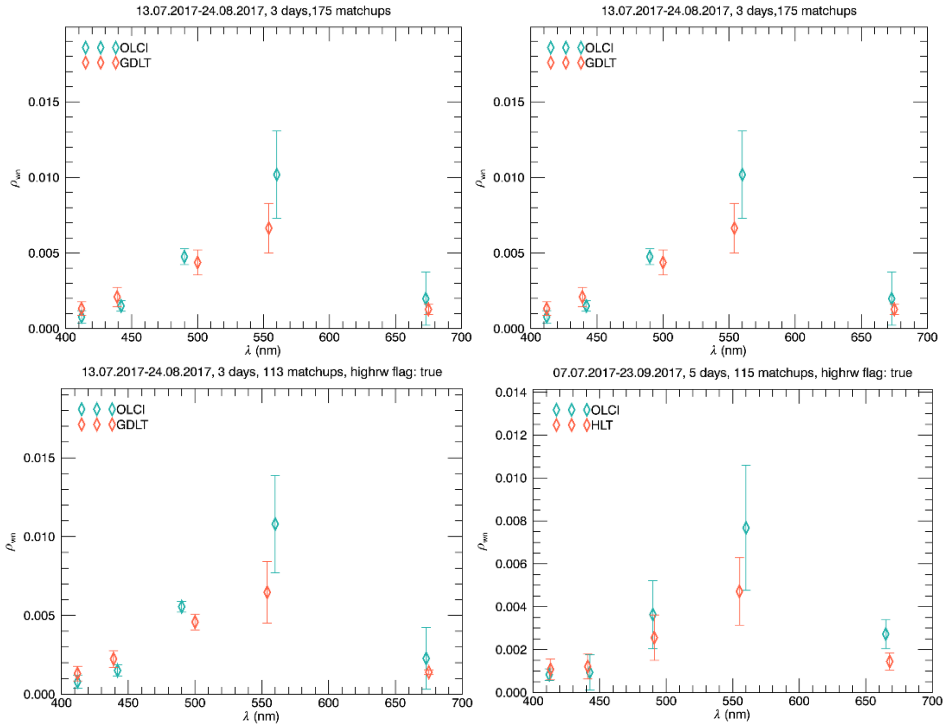

Figure 40: Normalized water leaving-reflectance (ρ_{WN}) averaged over 3 and 5 days from (green) OLCI and (red) the in-situ measurements from GDLT on the 13 & 31/07, 24/08 in 2017 (left) and HLT on the 7, 14 & 27/07, 14/08, 23/09 in 2017 (right). Applied OLCI flags (top) RHWNEG_b and (bottom) RHWNEG_b and WQSF_lsb_HIGHRW are raised

Although OLCI underestimates the value of ρ_{WN} compared to in-situ measurement for wavelength below 500nm and the opposite being noticeable above 560 nm, an important scattering of OLCI's estimation could be observed wrt in-situ measurements (Figure 40). In general, OLCI overestimates ρ_{WN} comparing

to the in-situ measurements averaged over all the 9*9 pixels matchups (

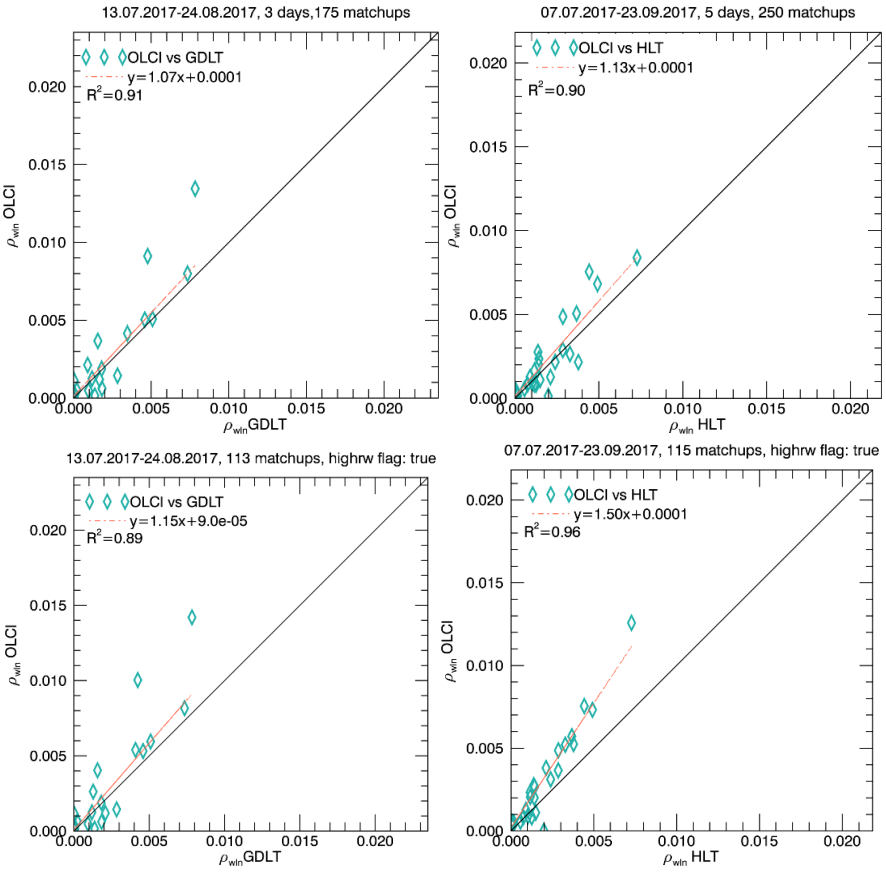

Figure 41: upper row). The |RDP| values shown inFigure 42, reach maxima of 30-40% for both sites.

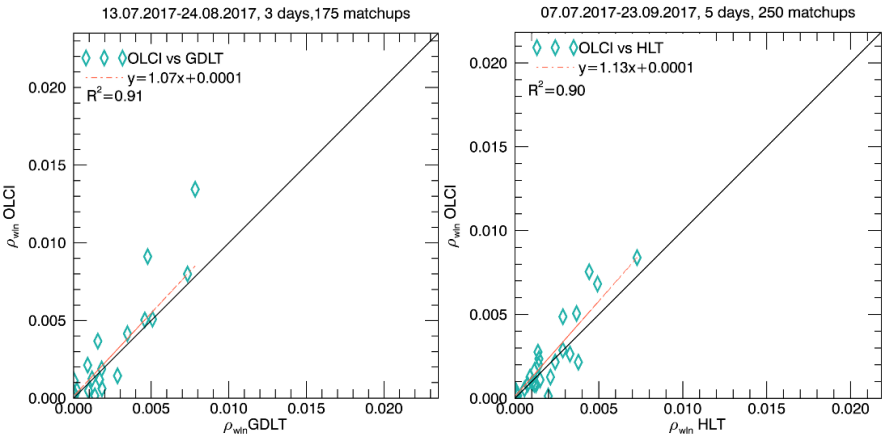

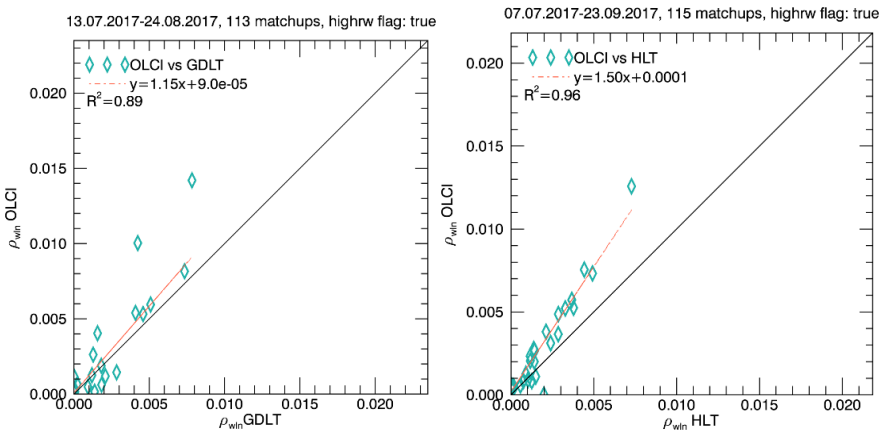

Figure 41: Regression plots of ρ_{WN} (OLCI/InSitu) over the 9*9 pixels matchups for GDLT on the 13 & 31/07, 24/08 of 2017 (left) and HLT on the 7, 14 & 27/07, 14/08, 23/09 of 2017 (right). Applied OLCI flags (top) RHWNEG_b and (bottom) RHWNEG_b and WQSF_lsb_HIGHRW are raised.

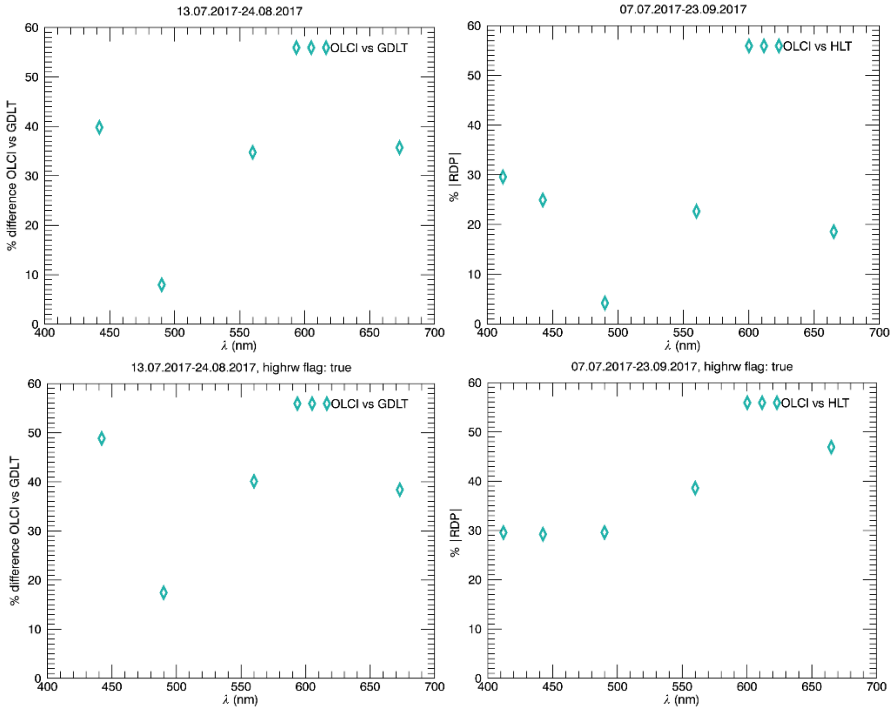

Figure 42: Absolute relative percent difference of OLCI L2 ρ_{WN} estimations with in-situ measurements from GDLT on the 13 & 31/07, 24/08 of 2017 (left) and HLT on the 7, 14 & 27/07, 14/08 and 23/09 of 2017 (right). Applied OLCI flags (top) RHWNEG_b and (bottom) RHWNEG_b and WQSF_lsb_HIGHRW are raised.

The differences between OLCI and in-situ measurements in these areas can result from a combination of systematic effects in the in-situ measurements as well as inaccuracies in the algorithms used to build L2 OLCI products *[S3 handbook].* In particular, in this coastal area, discrepancies at short wavelengths are likely to be linked with adjacency effects and limitations of the validity of the aerosol models and atmospheric correction algorithms near the coast. Indeed, the local aerosols may not be well

represented by the operational aerosol model, as optically complex waters may trigger components of the atmospheric process *[Franz et al 2007].* This is especially true in coastal areas dominated by CDOM and a low aerosol load of continental origin, as it is the case for the GDLT and HLT locations. In addition, those optically complex waters exhibit a lack of correlation between their optically significant constituents *[Gordon & Morel 1983]*, which tend to affect the accuracy of remote sensing products and likely impacts the accuracy of measurement *[Zibordi et al 2009b]*. In this study, those effects are likely to be due to high spatial/temporal variability of seawater optical properties within and between the OLCI and in-situ measurement, the bottom reflectance due to shallow waters (13 and 16 m respectively). Adjacency effects are also expected, due to the high albedo of the nearby mainland with respect to that of the sea, likely to lead to overestimations in both satellite and in-situ data products *[Zibordi et al 2009b].*

The impact of the *WQSF_lsb_HIGHRW flag*, triggering the waters case 2 and case 1 OLCI L2 processors has also been considered in this study. Indeed, it has been shown that processing data using waters case 1 or 2 algorithms can have a strong impact, in particular at short wavelengths in coastal areas, as discussed in *[Melin & Vantrepotte 2015]*. The percent of pixels where the *WQSF_lsb_HIGHRW flag* has been raised in both areas is shown below in Table 5 and Table 6. On average, 52% of the pixels are considered as case 2 in the 9x9 pixel's matchups around GDLT, and only 28.6% around HLT.

The impact of the *WQSF_lsb_HIGHRW* flag on the ρ_{WN} can be noticed on the average ρ_{WN} in Figure 40 and Figure 41. As noticeable, the case 1 algorithm tends to underestimate ρ_{NW} compared to GDLT and HLT in-situ measurements below 490 nm. Generally, case 1 OLCI matchups tend to give lower values than case 1+2 OLCI matchups. The rise of the case 2 *WQSF_lsb_HIGHRW flag* has a particularly strong impact at 490 and 560 nm, with an increased overestimation of OLCI ρ_{NW} compared to in-situ measurements. The scatter plots in Figure 41 confirm these trends. The |RDP|, appearing in Figure 42 are increased respectively by 50% and 30% around GDLT and HLT at 560nm when considering only the case 2 (*WQSF_lsb_HIGHRW flag: true*) pixels.

It seems that the raised *WQSF_lsb_HIGHRW* flag contributes to the observed overestimation of ρ_{WN} by OLCI around GDLT and HLT above 490 nm.

Figure 43 shows the total suspended matter from two different days were the number of case 2 pixels is high. However the integrated water vapour, aerosol T865 and A865 in the areas reach high levels, especially the TSM, with high peak noticeable along the coasts and at the rivers' mouths, consistent with Case 2 water *[Zibordi 2009 a, Darecki & Stramski 2004, Hojersley & Aas 2001]*.

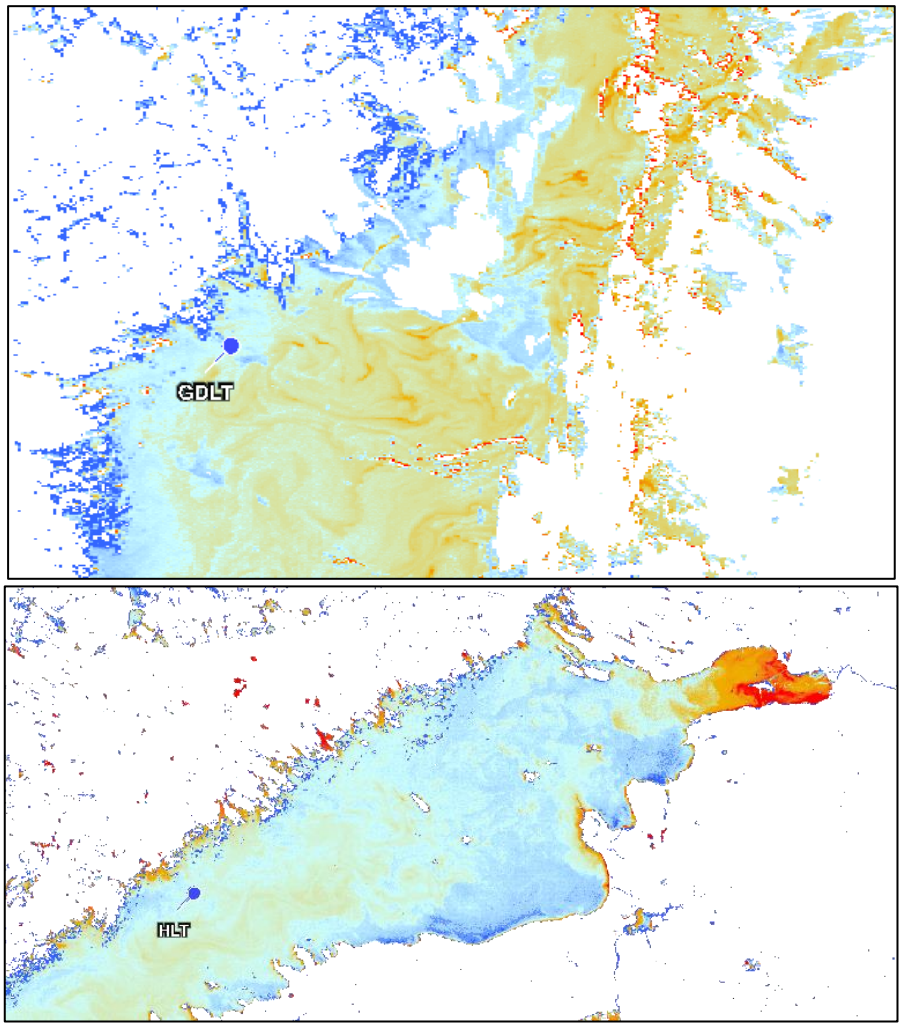

Figure 43: Total suspended matter concentration, estimated from OLCI L2 around GDLT on the 31/07/2017 (top) and HLT on the 14/08/2017 (bottom).

Table 5: auxiliary data for OLCI around GDLT location.

date	% pixels (highrw flag true)	IWV ($kg.m^{-2}$)	TSM ($mg.m^{-3}$)	A865	T865	Ch. NN ($mg.m^{-3}$)	Ch. Oc4me ($mg.m^{-3}$)	Ch.in-situ ($mg.m^{-3}$)
07.05.2016	55	6.61	0.30	0.27	0.39	0.67	4.81	1.88
14.06.2016	25	10.62	0.80	0.24	0.41	0.63	21.57	2.80
13.07.2017	32	24.62	2.24	0.37	0.17	10.35	2.52	1.36
31.07.2017	61	20.10	5.30	1.34	0.05	12.58	2.92	2.48
24.08.2017	87	18.26	1.08	1.42	0.14	5.52	0.50	2.61

Table 6: auxiliary data for OLCI around HLT location.

date	% pixels (highrw flag true)	IWV ($kg.m^{-2}$)	TSM ($mg.m^{-3}$)	A865	T865	Ch. NN ($mg.m^{-3}$)	Ch. Oc4me ($mg.m^{-3}$)	Ch. in-situ ($mg.m^{-3}$)
07.07.2017	6	25.07	3.34	1.41	0.03	7.88	4.36	2.21
14.07.2017	7	22.05	2.94	0.60	0.09	12.90	6.12	2.49
27.07.2017	17	5.28	2.03	0.41	0.30	23.44	4.05	4.61
14.08.2017	4	28.41	3.72	1.30	0.02	6.48	5.11	5.54
23.09.2017	14	29.21	1.24	0.70	0.19	0.0	3.23	15.03

2) Long Island Sound

OLCI L2 estimation of ρ_{WN} shows similar behavior as the in-situ measurement over LISCO site (Figure 40). The spectrum features are consistent with the one of case 2/turbid coastal water, dominated by color dissolved organic matter (CDOM) and a low aerosol load of continental origin, similar to the results obtained in oceanic areas by [Zibordi et al 2009b, Melin & Vantrepotte 2015]. Around LISCO location, the *TIDAL* flag is raised for all the OLCI pixels, consistent with the high concentration of total suspended matter (TSM), susceptible to be stirred by the tides. Values for the TSM content in Table 7 are also consistent with the case 2 water with tidal stirred sediments, explained both by the tidal effect on sediment and by the large input of fresh water from rivers rich in humus substances, shown in Figure 43. In general, OLCI overestimates ρ_{WN} comparing to the in-situ measurements averaged over all the 5x5 pixels matchups (Figure 40). The |RDP| values shown in Figure 41, reach maxima of ~40%.

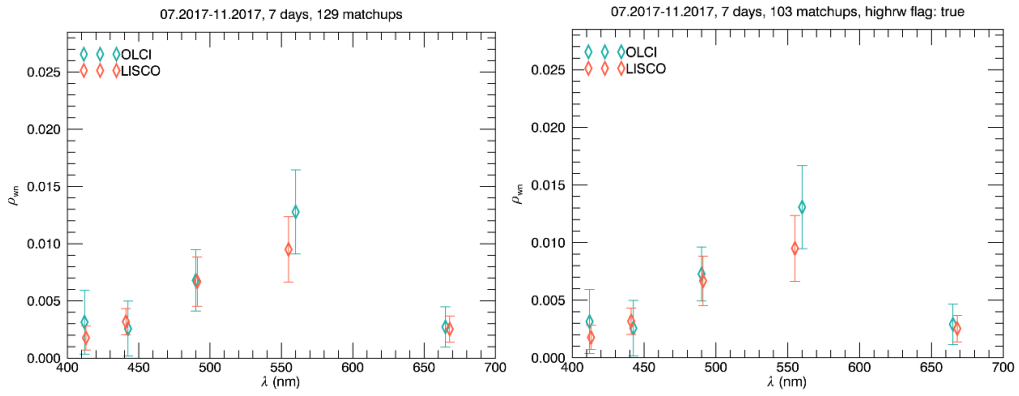

Figure 44: Normalized water leaving-reflectance (ρWN) averaged over OLCI and the in-situ measurements from LISCO on the 09/07, 01 & 31/08, 04 & 08/09, 21 & 28/11 of 2017. Applied OLCI flags (left) RHWNEG_b and (right) RHWNEG_b and WQSF_lsb_HIGHRW are raised

Table 7: auxiliary data for OLCI around LISCO location in 2017.

date	% pixels highrw raised	IWV ($kg.m^{-2}$)	TSM ($mg.m^{-3}$)	A865	T865	Chl.-a OC4Me ($mg.m^{-3}$)	Chl.-a NN ($mg.m^{-3}$)	Chl-a in situ ($mg.m^{-3}$)
07/09	96	24.6	3.8	0.4	0.06	8.0	2.3	6.6
01/08	88	40.9	9.7	1.5	0.09	22.7	5.8	7.2
31/08	96	48.3	2.5	0.6	0.29	10.2	0.6	4.1
04/09	28	27.6	1.1	0.6	0.23	20.2	0.4	6.8
08/09	12	34.2	2.7	0.9	0.11	13.0	2.7	4.4
21/11	88	17.2	4.7	1.1	0.05	6.2	1.7	3.5
28/11	96	40.1	2.3	0.5	0.04	5.1	2.4	3.4

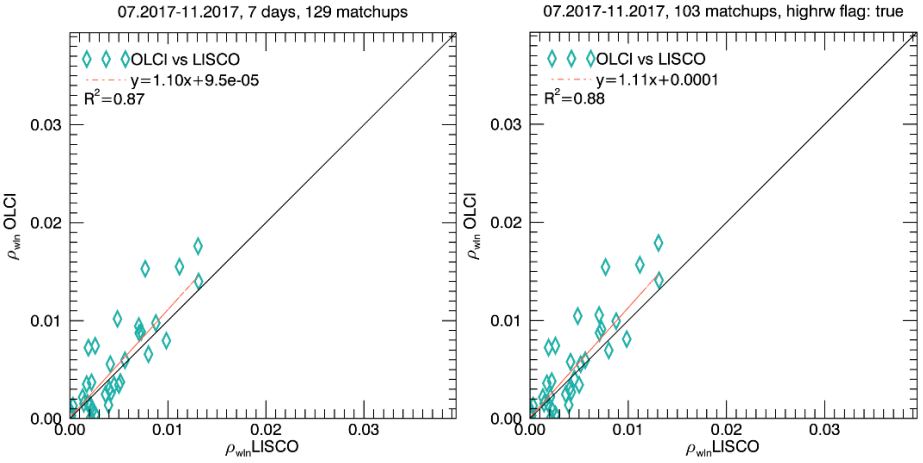

Figure 45: Regression plots over the 5x5 matchups for OLCI L2 and the in-situ measurements of ρWN at LISCO on the 09/07, 01 & 31/08, 04 & 08/09, 21 & 28/11 of 2017. Applied OLCI flags (left) RHWNEG_b and (right) RHWNEG_b and WQSF_lsb_HIGHRW are raised.

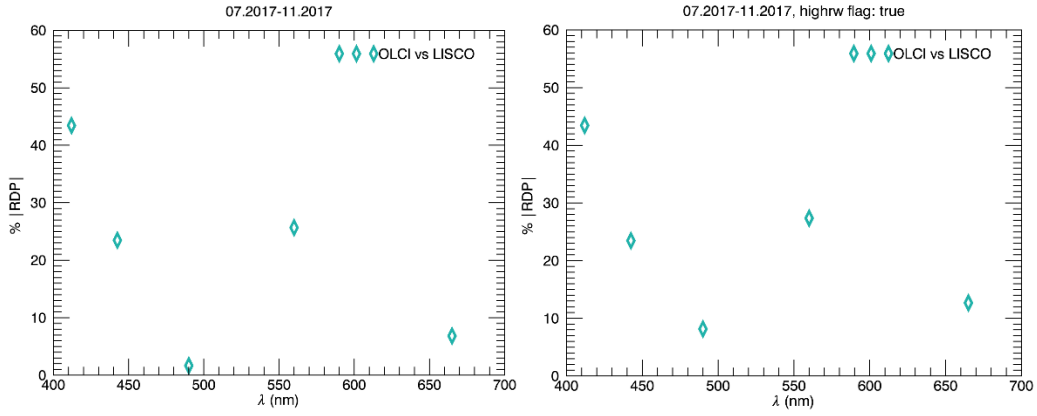

Figure 46: Absolute relative percent difference of OLCI L2 ρWN estimations with in-situ measurements from LISCO on the 09/07, 01 & 31/08, 04 & 08/09, 21 & 28/11 of 2017. Applied OLCI flags (left) RHWNEG_b and (right) RHWNEG_b and WQSF_lsb_HIGHRW are raised

Same as for GDLT and HLT sites, the differences between OLCI and in-situ measurements in LISCO area can result from a combination of systematic effects in the in-situ measurements as well as inaccuracies in the algorithms used to build L2 OLCI products *[S3 handbook].* In particular, in this coastal area, discrepancies at short wavelengths are likely to be linked with adjacency effects and limitations of the validity of the aerosol models and atmospheric correction algorithms near the coast. Indeed, the local aerosols may not be well represented by the operational aerosol model, as optically complex waters may trigger components of the atmospheric process *[Franz et al 2007].* In addition, those optically complex waters exhibit a lack of correlation between their optically significant constituents *[Gordon & Morel 1983]*, which tend to affect the accuracy of remote sensing products and likely impacts the accuracy of measurement *[Zibordi et al 2009b]*. Adjacency effects are also expected, due to the high albedo of the nearby mainland with respect to that of the sea *[Zibordi et al 2009b]*, likely to lead to overestimations in both satellite and in-situ data products.

The impact of the *WQSF_lsb_HIGHRW flag*, triggering the cases 1 and 2 water OLCI L2 processors has also been considered in this study. Indeed, it has been shown that processing data using cases 1 or 2 water processors can have a strong impact, in particular at short wavelengths in coastal areas, as discussed in *[Melin & Vantrepotte 2015]*. The percent of pixels where the flag *WQSF_lsb_HIGHRW* has been raised is shown in Table 7. On average, 72% of the pixels are processed as case 2 water pixels in the 5x5 pixel's matchups around LISCO.

The impact of the *WQSF_lsb_HIGHRW flag* on the ρ_{WN} can be noticed on the average ρ_{WN} in Figure 40. Generally, it seems that the raised *WQSF_lsb_HIGHRW* flag contributes to the observed overestimation of ρ_{WN} by OLCI around LISCO above 490 nm. These trends are confirmed by the scattering plots in Figure 41, and the |RDP| is increased around LISCO for pixels where the flag WQSF_*lsb_HIGHRW* is raised (Figure 42).

Figure 43 shows the high values of the total suspended matter content with high peak along the coast, consistent with case 2 water *[Zibordi et al 2009a]*.

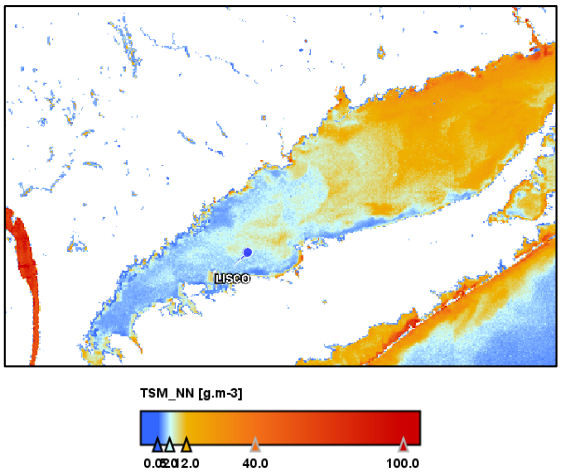

Figure 47: Total suspended matter concentration, estimated from OLCI L2 around LISCO on the 21/11/2017

5.3 [OLCI-L2WLR-CV-510 & 520] – Cloud Masking & Surface Classification for Water Products

There has been no update of the Cloud Masking & Surface Classification for Land Products during Cycle 026. Last figures (cycle 24) are considered valid.

5.4 [OLCI-L2WLR-CV530] Validation of Aerosol Product

There has been no new result during the cycle. Last figures (cycle 24) are considered valid.

5.5 [OLCI-L2WLR-CV-380] Development of calibration, product and science algorithms

There has been no new developments on **calibration, product and science algorithms** during the cycle

6 Validation of Integrated Water Vapour over Land & Water

There has been no new result during the cycle. Last figures (cycle 24) are considered valid.

7 Level 2 SYN products validation

7.1 [SYN-L2-CV-100]

There has been no new result during the cycle. Last figures (cycle 25) are considered valid.

8 Events

Two OLCI Radiometric Calibration Sequences have been acquired during Cycle 026:

- S01 sequence (diffuser 1) on 25/12/2017 12:41 to 12:43 (absolute orbit 9664)
- S01 sequence (diffuser 1) on 10/01/2018 19:09 to 19:11 (absolute orbit 9896)

9 Appendix A

Other reports related to the Optical mission are:

- S3-A SLSTR Cyclic Performance Report, Cycle No. 026 (ref. S3MPC.RAL.PR.02-026)

All Cyclic Performance Reports are available on MPC pages in Sentinel Online website, at: https://sentinel.esa.int

End of document